

Reversible fluxon logic: Topological particles allow ballistic gates along one-dimensional pathsW. Wustmann¹ and K. D. Osborn^{1,2,*}¹*The Laboratory for Physical Sciences, College Park, Maryland 20740, USA*²*The Joint Quantum Institute, University of Maryland, College Park, Maryland 20742, USA*

(Received 20 April 2017; revised manuscript received 20 October 2019; published 31 January 2020)

As we reach the end of Moore’s law, digital logic uses irreversible logic gates whose energy consumption has been scaled toward a lower limit. Reversible logic gates can provide a dramatic energy-efficient alternative, but rely on reversible dynamics. Here, we introduce a set of superconducting reversible gates that are powered alone by the inertia of the digital input states, contrasting existing adiabatic prototypes which are powered by an external adiabatic drive. The classic model of an inertia-powered reversible gate uses ballistic particles which scatter in two dimensions, where the digital state is represented by the particle path. Our ballistic gates use as the bit state the topological charge (polarity) of a fluxon moving along a long Josephson junction (LJJ) such that the particle path is confined to one dimension. The fundamental structures of our reversible fluxon logic (RFL) are one-bit gates which consist of two LJJs connected by a circuit interface that comprises three large-capacitor Josephson junctions (JJs). Numerical simulations show how a fluxon approaching the interface under its own inertia converts its energy to an oscillating evanescent field, from which in turn a new fluxon is generated in the other LJJ. We find that this resonant forward scattering of a fluxon across the interface requires large capacitances of the interface JJs because they enable a conversion between bound-evanescent and traveling fluxon states (without external power). Importantly, depending on the circuit parameters, the new fluxon may have either the original or the inverted polarity, and these two processes constitute the fundamental identity and NOT operations of the logic. Based on these one-bit RFL gates, we design and study a related two-bit RFL gate which shows that fluxons can exhibit conditional polarity change. Energy efficiency is accomplished because only a small fraction of the fluxon energy is transferred to modes other than the intended fluxon. Simulations show that over 97% of the total fluxon energy is preserved during gate operations, in contrast to irreversible gates where the entire bit energy is consumed in bit switching. To provide insight into these phenomena, we analyze the one-bit gate circuits with a collective-coordinate model which describes the field in each LJJ as a combination of fluxon and mirror antifluxon. This allows us to reduce the many-junction circuit (the three interface JJs and the many JJs approximating the LJJs, solved numerically) to that of two coupled degrees of freedom that each represent a particle. The evolution of the reduced model agrees quantitatively with the full circuit simulations and validates the use of the mirror-fluxon ansatz. Parameter tolerances are calculated for the proposed circuits and indicate that RFL gates can be manufactured and tested.

DOI: [10.1103/PhysRevB.101.014516](https://doi.org/10.1103/PhysRevB.101.014516)**I. INTRODUCTION**

Today’s conventional digital logic is based on irreversible gates. Physically, the irreversibility arises in a gate due to the energy that is dissipated in switching processes between the states representing the logic bits. This energy cost is generally set by the energy of the digital state itself: the charging energy of a voltage state in semiconductor logic or the magnetic energy of a flux state in conventional superconducting logic. In both cases, sufficiently large damping ensures deterministic and fast state switching compatible with GHz processing speeds. Unlike complementary-metal-oxide-semiconductor (CMOS) gates, however, the intrinsic damping in superconducting circuits is very small, allowing nearly dissipationless reversible dynamics. As a result, superconducting circuits also allow for the implementation of both quantum logic and reversible digital logic. The most common

type of reversible digital logic is “adiabatic reversible logic,” where state switching uses an external waveform (or clock) to steer an adiabatic state evolution in the absence of large damping. Here, we report on an unusual gate class known as ballistic reversible gates, which are powered by the inertia of the incoming bits. Specifically, we find that fluxons can undergo energy-conserving transformations of polarity and this mechanism can be used for ballistic reversible logic gates.

Industrial development of microelectronics has long benefited from transistor density scaling which allows the vast improvements described by Moore’s law. However, the related performance scaling has slowed down considerably in recent years and is expected to come to an end soon. One particular limiting factor is the heat generated during CMOS transistor switching in logic gates [1,2]. These logic gates are irreversible from an information perspective because they do not perform one-to-one maps of input-to-output states. Their energy cost includes Landauer’s entropy cost of $\ln(2)k_B T$ for the erasure of each bit of information at temperature T . Although the bit switching energy of irreversible gates could

*osborn@lps.umd.edu

in principle be this small, in practice it consumes the entire energy of the bit state itself (e.g., the voltage state) through fast damping in order to enable GHz processing speeds. For reasons that include thermal stability and state distinction, the bit state energy has to be $\gg k_B T$ (e.g., $>1000k_B T$), and consequently the switching energy exceeds Landauer's entropy cost by orders of magnitude in practice. Similar principles hold for conventional single-flux quantum (SFQ) logic in superconducting circuits. SFQ logic uses a flux quantum generated by a persistent current in a quantizing loop to represent one-bit state. Bit switching, i.e., the change of the flux state in the loop, is enabled by a Josephson junction (JJ); once the total current acting on a JJ exceeds its critical current I_c , it undergoes a rapid 2π -phase change. Equilibrium is reestablished through a damping resistor that shunts the JJ [3]. Similar as in the CMOS bit switching, the dissipated energy here is on the order and larger than the bit energy of the flux quantum itself; specifically, the switching energy is $\sim I_c \Phi_0$, where Φ_0 is the superconducting flux quantum. One such recently developed (irreversible) SFQ logic type [4–6] allows 2π -phase switching at an energy of only $I_c \Phi_0 \approx 1300k_B T$.

Reversible logic gates provide an alternative approach to computing. These gates produce no entropy related to bit erasure since they perform one-to-one mapping of input-to-output states. A corresponding theoretical model for a reversible computer was established decades ago [7]. To provide an advantage over irreversible logic, reversible gates must use dynamics that conserves most of the bit-state energy. This can be achieved within an adiabatic model, developed by Likharev [8], by using externally applied fields that adiabatically modulate the circuit potential. Arriving later than their quantum counterparts in superconductivity, reversible digital logic has been demonstrated more recently in circuits, which include N-SQUID [9] and reversible Quantum Fluxon Parametron (QFP) [10]. According to Likharev's adiabatic model, energy dissipation varies proportional to the modulation frequency [8,11] and thus can be made arbitrarily small as the speed is lowered.

Although demonstrated reversible gates are of the adiabatic (reversible) logic type, a physically distinct type known as ballistic gates can be studied. These make use of scattering processes and are solely powered by the initial energy of the digital state. This is apparent in the original "billiard ball model" [12]: particles moving under their inertia collide with each other and with reflective boundaries of a well-defined two-dimensional (2D) gate geometry. The resulting paths taken by the particles encode the digital output state of the gate. Ballistic gates have been studied using soliton propagation within fibers [13] or 2D layered media [14]. A technical challenge in this type of reversible logic is that they must be correctable for path perturbations in 2D and desynchronization errors [15], and here we will address the former.

In this work we introduce gates for efficient ballistic reversible logic in superconducting circuits under the name of reversible fluxon logic (RFL). This approach uses fluxons and antifluxons in long Josephson junctions (LJJs) to represent the two-bit states. A fluxon, or flux soliton, is a spatially extended topological excitation of the LJJ and carries a quantized magnetic flux Φ_0 ($-\Phi_0$ in case of an antifluxon). In RFL the LJJs form fluxon waveguides and are connected at

circuit interfaces. Fluxon gates can be made of these structures where a fluxon scatters from one LJJ to another through a resonant nonlinear process. Through numerical simulation of the gate circuits we find cases where an incoming fluxon excites resonant dynamics of the coupled LJJs which results in the net forward scattering of the fluxon to another LJJ. In these nonlinear processes, the character of the incoming fluxon changes near the interface where it turns into a localized interface excitation with evanescent fields in the LJJs. From this localized state, a new ballistic fluxon forms afterward in the other LJJ. For this 1D scattering, no path corrections are required in contrast to the original (2D) ballistic gate model.

Importantly, while the fluxon number is conserved, the scattering can result in the transformation of a fluxon into an antifluxon (or vice versa), and this change of polarity provides a means for bit switching (defined as a NOT gate). This is fundamental because the fluxon polarity represents a topological charge which cannot change in a planar LJJ [only along a LJJ that is twisted in three dimensions (3D)]. The NOT gate occurs in a one-bit structure which has three JJs in the interface. For different parameters of these interface JJs the dynamics changes; in particular, the gate type can be changed to an identity (ID) gate, where fluxon polarity is preserved but the resonance is changed. In related two-bit gates, the fluxon polarities induce a conditional polarity change. The bit switching in RFL involves a (gradual) undamped 4π -phase change of an interface JJ. The 4π change is thus found to be enabled by resonance between LJJs, and it contrasts adiabatic reversible logic which generally uses a $\sim 2\pi$ -phase change, related to neighboring minima of the JJ potential [8].

The RFL gate interface is designed to ensure that an incoming fluxon (with a given velocity and for given LJJs) is coherently transformed into the local interface excitation and back into another forward-moving fluxon in a different LJJ. To accomplish this, the ends of the LJJs near the interface must behave differently than in bulk. In particular, we find that relatively large (added shunt) capacitances of the interface JJs are crucial to the resonant scattering present in the one- and two-bit gates. We have designed the RFL gates for relatively high incoming fluxon velocities of around $0.6c$, where c is the upper (relativistic) velocity limit.

The RFL gates presented in this study are reversible in the sense that their energy cost is only a small fraction of the digital state energy. In our simulations, an output fluxon can obtain 97% of the energy of the input fluxon. The gates can also be logically reversible at lower efficiency, which allows some tolerance to imperfect structures. The remaining small fraction of initial energy is dissipated to the environment of the gate in the form of small-amplitude plasma waves in the LJJs. The JJs in the simulations are undamped. Beyond this general property of superconducting circuits, we note that the observed high-energy retention in the fluxon degree of freedom is a speciality of our resonant logic gates. Also, the RFL gates have a gate time of only a few Josephson oscillation periods, $T_{\text{gate}} \sim 1/\nu_J$, where ν_J is the natural frequency in the LJJ. In principle, ν_J could be on the order of tens of GHz for fast processing speeds.

The complex scattering dynamics observed at the circuit interfaces in an RFL gate goes beyond the usual fluxon perturbation theory [16]. While the latter assumes the fluxon's

integrity (possibly allowing for internal excitations, shape modes, etc.), in our case the fluxon breaks up at the interface and its energy is converted into an interface oscillation mode. This mode involves an excitation of the interface JJs but also has finite amplitude in the adjacent LJJs, decaying away from the interface. The LJJs therefore play a role not only as input and output ports, but also as integral parts of the gate itself. To analyze the nonperturbative scattering dynamics, we parametrize the fields in each LJJ as a superposition of a fluxon paired with a mirror antfluxon. This collective coordinate (CC) model can account for the various scattering processes with conserved energy, including those where the fluxon polarity changes. In case of the one-bit RFL gates, for example, the Lagrangian produces coupled dynamics in two coordinates. The dynamics can thus be thought of as a possible excitation in one LJJ interacting with a possible excitation in the other LJJ, where each has an independent spatial coordinate along its LJJ. The CC dynamics accurately reproduces dynamics from the full gate simulation. The forward scattering with and without polarity change are seen to arise from the special form of the effective potential and essential mass-gradient forces generated by the interface. The mass-gradient forces, not used in other SFQ logic, are introduced in our superconducting digital gates through engineered capacitances.

The interface scattering of the fluxon may be compared with scattering of a fluxon at a point defect in an LJJ [17,18], or at a qubit-generated perturbation potential [19–22]. In those situations, the moving fluxon interacts with a small-amplitude bound state at the defect. Above a critical velocity the fluxon is transmitted, but a slow fluxon may be backscattered or trapped. Unlike in these systems, our system allows polarity change of a fluxon. This is here made possible since one of the superconducting electrodes of the LJJ is interrupted in the interface by a JJ. This JJ can undergo large phase winding in resonance, corresponding to a change of the flux inside the LJJ, e.g., by two flux quanta in case of the NOT gate. Moreover, we typically find that the outcome of scattering at the interface depends only moderately on the incoming velocity, in contrast to fluxon scattering at point defects for which high sensitivity to the incoming fluxon velocity had been found [17].

Building on the results for the one-bit gates, we have also designed and simulated two-bit gate structures which are found to allow conditional polarity changes for the two incoming fluxons. In this particular two-bit gate, a controlled NOT SWAP (NSWAP), the coupled dynamics of the two input fluxons is symmetry related to the dynamics of two different uncoupled one-bit gates. Depending on the relative polarity of the two input fluxons, it conditionally produces a NOT or ID operation. This two-bit gate has an interface with seven capacitance-shunted JJs. This work covers an initial set of RFL gates. Subsequent work describes how to store and launch fluxons for the purpose of synchronization and resupply of energy between gates [23]. Reference [23] also uses a two-bit gate named IDSN with similar dynamics as in the here presented gates, as a key component of an efficient CNOT gate.

The paper is organized as follows: In Sec. II we introduce the gate circuit and briefly describe the main results for the fluxon logic gates. We start by presenting numerical

simulations of circuits with fluxon dynamics in the one-bit gate structures. We then analyze the fluxon dynamics in these gate structures by means of a collective coordinate (CC) model. It describes the fields near the interface as consisting of a fluxon paired with a mirror antfluxon (Sec. II C). From two one-bit gate types we then construct a two-bit gate which likewise is unpowered and reversible (Sec. II D). We further study dynamics of the two-bit gate embedded into a simulation test platform for fluxon launch and output state storage. This serves to show that the gates do not depend sensitively on a perfectly launched fluxon. Section III presents more detail on the CC model and its application to describe the fluxon scattering at the circuit interfaces, including such scattering that is not used for gates. This analysis provides a better intuition for the scattering dynamics and helps to identify the relevant parameter regimes for the gates. The precise interface parameters used in gates are calculated numerically in Sec. IV from a Monte Carlo optimization of parameters. The gate operation under changes of single parameters is calculated as well (parameter margins). In Sec. V we explain in detail the operation of the two-bit gate and how it can be mapped to equivalent one-bit gates, as it depends on the relative polarity of input fluxons. A conclusion is given in Sec. VI. The Appendix contains details of the gate analysis and shows that we expect negligible energy loss from fluxons in our LJJs due to the small LJJ-model discreteness.

II. OPERATION AND ANALYSIS OF GATES

A. One-bit gate system

We study the dynamics of a fluxon in a superconducting circuit as sketched in Fig. 1(a). It consists of two discrete LJJs at $|x| \geq a/2$. These are made from an array of Josephson junctions (JJs), with parallel critical current I_c and capacitance C_J , connected to their neighbors through cell inductance L . Each LJJ ends at an interface Josephson junction of capacitance and critical current (\hat{C}_J, \hat{I}_c) . The termination junctions (\hat{C}_J, \hat{I}_c) of two LJJs are connected in a series loop with two other elements: a central interface junction of (C_J^B, I_c^B) , and an inductor \hat{L} . Elements (C_J^B, I_c^B) , (\hat{C}_J, \hat{I}_c) , and \hat{L} with their connections constitute the interface cell.

We simulate the dynamics by numerically integrating the $N + 1$ equations of motion for the junction phase differences: ϕ^B for the center-interface junction, and ϕ_n for the $1 \leq n \leq N_l$ and $N_l + 1 \leq n \leq N$ junctions in the left and right half of the circuit, respectively, where the phases of the left and right interface junctions are $\phi_L = \phi_{N_l}$ and $\phi_R = \phi_{N_l+1}$. The equations of motion are generated by the Lagrangian

$$\begin{aligned} \mathcal{L} = & \left(\frac{\Phi_0}{2\pi} \right)^2 \left[\sum_n \frac{C_{J,n}}{2} (\dot{\phi}_n)^2 + \frac{C_J^B}{2} (\dot{\phi}^B)^2 \right] \\ & - \left(\frac{\Phi_0}{2\pi} \right) \left[\sum_n I_{c,n} (1 - \cos \phi_n) + I_c^B (1 - \cos \phi^B) \right] \\ & - \frac{1}{2} \sum_n [L_n^A (I_n^A)^2 + L_n^B (I_n^B)^2]. \end{aligned} \quad (1)$$

As defined above, there are identical junctions ($C_{J,n} = C_J$, $I_{c,n} = I_c$) and inductors $L_n = L$ in the LJJ cells. Also, the

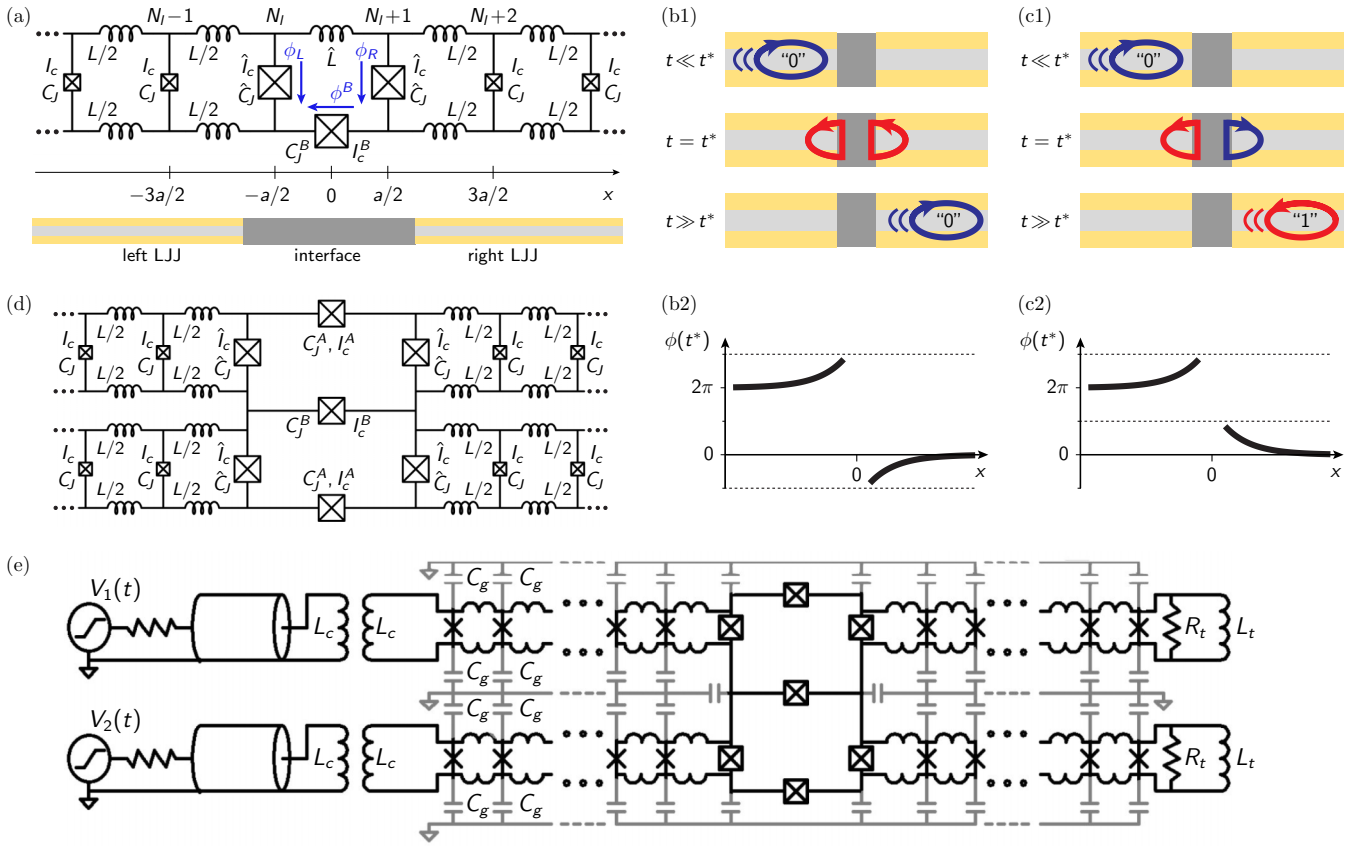


FIG. 1. (a) General one-bit gate circuit composed of two LJJs ($n \leq N_l - 1$ and $\geq N_l + 2$) and an interface that contains JJs with phases ϕ_L , ϕ_R , and ϕ^B . Depending on the interface parameters (capacitances and critical currents of interface JJs, inductance), the structure allows various types of fluxon dynamics, including the resonant forward scattering to be employed in RFL gates. As indicated in the diagram below, the LJJs with cell inductance L and critical current I_c are discrete versions of continuous LJJs (yellow and light gray JJ trilayer boxes) with inductance and critical current per unit length L/a and I_c/a and $a \rightarrow 0$. (b), (c) An illustration of one-bit gate phenomena found in numerical solutions, using a free traveling fluxon as an initial condition (initially several Josephson penetration depths away from the interface). Fluxons and antifluxons encode the bit states “0” and “1.” Currents are shown at the scattering symmetry time t^* , as well as before and after, for the ID gate (b1) and the NOT gate (c1). Panels (b2) and (c2) show the LJJ-phase profiles at t^* , indicating the then excited localized state with evanescent fields into the bulk of the LJJs. The corresponding numerical solutions are shown in Figs. 2 and 3, and solutions of an analytical model in Fig. 4. (d) Two-bit gate circuit consisting of two input and two output LJJs connected by an interface. Figure 5 shows the simulated operation of a specific two-bit gate (NSWAP). (e) Two-bit gate circuit (central part) in a simulation test platform. The platform allows simulations of gates with nonideal fluxon launch: voltage steps created in the transmission lines launch fluxons into the inductively coupled LJJs. A ground plane (gray wires) adds stray capacitance. The fluxons move toward the gate where they interact. A successful gate will result in forward-scattered fluxons, which then induce circulating currents in the storage loop (right) for possible readout. The simulated operation of a specific two-bit gate (NSWAP) in the test platform is shown in Fig. 6.

left and right interface junctions have $C_{J,N_l} = C_{J,N_l+1} = \hat{C}_J$ and $I_{c,N_l} = I_{c,N_l+1} = \hat{I}_c$. Finally, the interface inductance and center junction have values $L_{N_l-1} = \hat{L}$ and (C_J^A, I_c^A) , respectively. The currents on the upper rail of the LJJs are given by $I_n^A = \Phi_0(\phi_{n+1} - \phi_n)/(2\pi L_n)$ ($n < N_l$, $n \geq N_l + 1$) and $I_n^B = -I_n^A$ on the lower, where $L_n = L_n^A + L_n^B$ is the total inductance of the n th LJJ cell. The current on the upper rail in the interface (with center inductor \hat{L}) is given by $I_{N_l}^A = \Phi_0(\phi_R - \phi_L + \phi^B)/(2\pi \hat{L}) = -I_{N_l}^B$, where $I_{N_l}^B$ is the current on the lower rail of the interface. The interface cell is symmetric in propagation direction (left-right), as required for a physically reversible gate.

When scaling the parameters $(L, C_J, I_c) \propto (a, a, 1/a)$, in the limit $a \rightarrow 0$ a continuous LJJ is realized rather than our approximate one. The dynamics of the continuous LJJ is

governed by the sine-Gordon equation (SGE) [16,24,25]

$$\ddot{\phi} - c^2 \phi'' + \omega_J^2 \sin \phi = 0. \quad (2)$$

The characteristic time and length scales of the LJJ are given by the Josephson frequency ω_J and Josephson penetration depth λ_J , defined by $\omega_J^2 = (2\pi/\Phi_0)I_c C_J^{-1}$ and $\lambda_J^2 = (\Phi_0/2\pi)a^2(LI_c)^{-1}$, where L/a and I_c/a are the LJJ inductance and critical current per unit length a . The upper bound for the group velocity in the LJJ is the Swihart velocity $c = \lambda_J \omega_J$.

In the (infinite) continuous LJJ a stable fluxon exists in form of the soliton solution to the SGE, with the phase and phase-derivative profiles

$$\phi^{(\sigma,X)}(x, t) = 4 \arctan \exp\{-\sigma[x - X(t)]/W\}, \quad (3)$$

$$\dot{\phi}^{(\sigma,X)}(x, t) = \frac{2\sigma\dot{X}}{W} \operatorname{sech}\{[x - X(t)]/W\}, \quad (4)$$

where $\phi(\Phi_0/2\pi)$ is the voltage across the LJJ. We choose the range $0 \leq \phi^{(\sigma, X)} \leq 2\pi$, and the polarity $\sigma = 1$ ($\sigma = -1$) for a fluxon (antifluxon) solution. Here, X is the center position of the fluxon, which propagates with constant velocity $v_0 = \dot{X}$ ($|v_0| < c$) and has a characteristic width $W = \lambda_J \sqrt{1 - v_0^2/c^2}$.

For use in a logic gate, a fluxon first needs to be created in an LJJ. In this context, Fig. 1(e) shows a schematic of a simple test platform for a two-bit gate, with two input and two output LJJs (the two-bit gate is discussed in Sec. IID, and in more detail in Sec. V). In addition to the two-bit gate itself, the platform provides components that allow one to (i) create ballistic fluxons in the input LJJs from coupled transmission lines and (ii) store flux at the end of each LJJ output for a gate readout (test). The fluxon launch in each input LJJ is initiated by ramping up the input voltage of a transmission line. Also, in the platform the LJJs and interface are additionally coupled via small capacitances to ground. We have successfully simulated the fluxon launch and the subsequent gate operations and flux storage of this test platform, as discussed in Sec. IID (cf. Fig. 6). In the interest of simplicity, simulations presented here are mainly performed only for the gate alone, without circuit components for launch, output flux storage, and capacitive coupling to ground.

In these simulations, a soliton is simply taken as the initial condition $\phi_n(t=0) = \phi^{(\sigma, X)}(x_n, 0)$. This is evaluated on the discrete lattice of the circuit $x_n = an - a(N_l + 1/2)$ ($n = 1 \dots N$), where a is the lattice spacing. Specifically, a fluxon is initialized in the left LJJ, $X(t=0) = X_0 < 0$, and is incident on the interface with initial velocity $\dot{X} = v_0 > 0$, and polarity $\sigma = 1$.

In an ideal continuous LJJ the fluxon energy $E_{\text{fl}} = 8E_0/\sqrt{1 - v_0^2/c^2}$ is conserved according to the SGE, where $E_0 = \Phi_0 I_c \lambda_J / (2\pi a)$. In a discrete LJJ the fluxon motion is in general damped because the discreteness forms a perturbation through which a moving fluxon can excite linear plasma modes of the (discrete) LJJ. (These wave modes are solutions of the linearized SGE.) The moving fluxon thus emits plasma waves and as a result loses energy [26–28]. However, this energy loss mechanism is strongly suppressed if $a/\lambda_J < 1$, and this criterion characterizes the regime of “small LJJ discreteness.” The LJJs used in this paper as part of the logic gates are chosen in this regime $(a/\lambda_J)^2 = 2\pi I_c L / \Phi_0 = 1/7$, where the energy loss of the moving fluxon is negligible. In Appendix A we briefly discuss the fluxon-energy loss rate at this (small) discreteness and its dependence on the initial fluxon velocity. For a typical initial velocity $v_0/c = 0.6$, the fluxon energy is $E_{\text{fl}} = 10E_0$, where 20% of E_{fl} is kinetic energy. As shown in Appendix A, in our LJJs such a fluxon loses only a fraction 10^{-7} of its energy in a time ω_J^{-1} due to the discreteness. This allows us to discuss the LJJs as nearly continuous in the context of the RFL gates, which are meant to operate over such short times.

B. Fluxon forward scattering for one-bit gates

The gate circuit of Fig. 1(a) supports equilibrium states of the form $\phi(x) = 2\pi K_L \Theta(-x) + 2\pi K_R \Theta(x)$ in the LJJ and $\phi^B = 2\pi(K_L - K_R)$ on the center-interface JJ, where $K_{L,R} \in \mathbb{Z}$ and $\Theta(x)$ is the Heaviside step function. Since we constrain studies to a parameter regime with $L < \Phi_0/(2\pi I_c^B)$, without

loss of generality we can disregard states with finite flux trapped in the interface cell [29], such that $\phi_L - \phi_R + \phi^B = 0$ in equilibrium. Taking $(K_L, K_R) = (0, 0)$ as the initial state, in fully inelastic scattering of an input fluxon, i.e., if the entire initial fluxon energy is exhausted in the interface region, the interface would settle into the equilibrium state $(K_L, K_R) = (1, 0)$. Inelastic scattering generally results from excitation of high-frequency plasma waves ($\omega > \omega_J$) at the interface which are radiated into the LJJs and thus spread the initial fluxon energy incoherently. The amount of radiation generated at the interface depends on the interface parameters. It is strongly suppressed in the following regimes, related to known scattering dynamics in an LJJ: (i) The fluxon is transmitted across the interface for $I_c^B \gg I_c$ and $C_J^B \ll I_c^B C_J / I_c$, while $\hat{I}_c \simeq I_c$, $\hat{C}_J \simeq C_J$, $\hat{L} \simeq L$, because the center-interface junction essentially acts as a small linear inductance due to the large I_c^B , and the entire circuit thus approximates a single LJJ. (ii) If the potential energy of the interface is too high, e.g., $\hat{I}_c \gg I_c$, the fluxon is reflected back before reaching the interface, similar to a shunt-terminated LJJ. (iii) The inter-LJJ coupling is suppressed due to the small C_J^B and I_c^B if $C_J^B \ll C_J$, $I_c^B \ll I_c$, $\hat{I}_c \simeq I_c$, $\hat{C}_J \simeq C_J$, and $\hat{L} \leq L$. This is comparable to an open terminated LJJ and thus the incident fluxon is scattered back elastically as an antifluxon, while the center-interface junction undergoes a 4π -phase winding. (Note that the interface cell does not store significant flux, but two flux quanta, $2\Phi_0$, must be exchanged between the interface cell and the environment.) These elastic processes involve transitions of the initial equilibrium state $(K_L, K_R) = (0, 0)$ in the interface region to (i) $(K_L, K_R) = (1, 1)$, (ii) $(K_L, K_R) = (0, 0)$, and (iii) $(K_L, K_R) = (2, 0)$, respectively.

Inelastic scattering and fluxon reflection are undesirable for efficient reversible gates. We therefore mainly report on reversible scattering phenomena where the fluxon energy is transferred into a coherent localized oscillation about the equilibrium state $(K_L, K_R) = (1, 0)$, and remarkably followed by the creation of a fluxon or antifluxon in the other LJJ as a resonant forward-scattering process.

In Fig. 2(b) numerically simulated dynamics of the LJJ phases $\phi_n(t)$ are shown vs position x_n and time t , for interface parameters given in the caption. The phases ϕ_n are also shown for specific times t in Figs. 2(a1)–2(a5). After moving ballistically (approximately freely) in the left LJJ, e.g., Fig. 2(a1), the fluxon energy is converted to a localized oscillation at the interface with evanescent fields into the LJJs, e.g., Figs. 2(a2)–2(a4). During that stage the characteristic phase profile of the original fluxon, Eq. (3), is destroyed. A large phase difference $\phi_L - \phi_R$ has accumulated between the left and right interface junctions $\phi_L = \phi_{N_l}$ and $\phi_R = \phi_{N_l+1}$. This is accompanied with an increase of the phase ϕ^B of the center-interface junction, shown in Fig. 2(c), such that the phase across \hat{L} remains small, $(\phi_R - \phi_L + \phi^B) \ll \pi$. During the localized oscillation, the field $\phi(x, t - t^*) - 2\pi \Theta(-x)$, measured relative to the equilibrium state $(K_L, K_R) = (1, 0)$, behaves parity-time antisymmetric where the symmetry time t^* is defined by $\dot{\phi}^B(t^*) = 0$. After the symmetry time t^* , we observe the energy from the local oscillation create a ballistic (unpowered) moving fluxon in the right LJJ (a5), while the interface region is left in the equilibrium state $K_L = K_R = 1$.

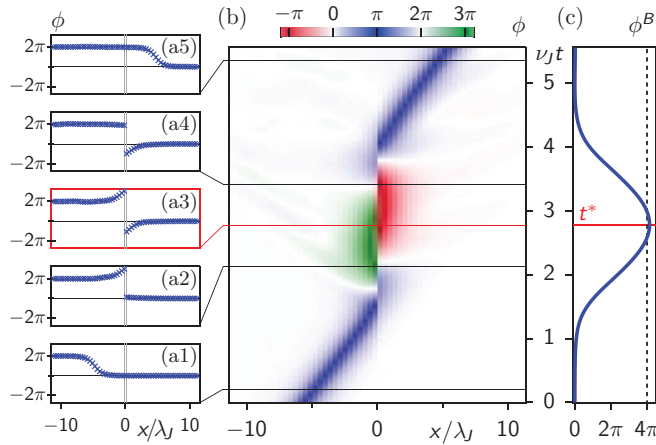


FIG. 2. Polarity-preserving ID gate realized with one-bit gate structure [Fig. 1(a)]: (a) LJJ phases ϕ_n vs x_n at specific times $|t - t^*| \sim 1/\nu_J$, where t^* is gate symmetry time and ν_J is the Josephson frequency. (b) Color representation of ϕ_n vs x_n and t , and (c) phase ϕ^B of center-interface junction, for fluxon incident on interface at $x = 0$ with initial velocity $v_0 = 0.6c$. In (b) the blue color of the fluxon trace at $x < 0$ and $x > 0$ indicates the same fluxon type. The interface parameters are $C_J^B/C_J = 6.0$, $I_c^B/I_c = 0.10$, $\hat{C}_J/C_J = 5.8$, $\hat{I}_c/I_c = 0.80$, and $\hat{L}/L = 0.06$, and we note that the center junction has negligible critical current (I_c^B) but significant capacitance (C_J^B).

The process is almost ideally elastic, with the new fluxon propagating at 96% of the initial velocity v_0 , and we note that no bias is present in the gate region (within several Josephson penetration depths of the interface). Compared to straight transmission across the interface, the new fluxon appears with a time delay of $T \approx 2.7(2\pi/\omega_J)$, within a factor of 3 of the Josephson period.

A different reversible forward scattering is illustrated in Fig. 3, for an interface that differs from that in Fig. 2 only by increasing C_J^B to $12.0C_J$. Coherent energy transfer again takes place from the incident fluxon to an interface oscillation which spans a time $T \approx 1.1(2\pi/\omega_J)$, approximately half of the process in Fig. 2. The field $\phi(x, t - t^*) - 2\pi\Theta(-x)$ exhibits parity-time symmetry with respect to a time t^* defined by $\phi^B = 2\pi$. Thus, after the oscillation, the interface region settles to the state with $K_L = 1$, $K_R = -1$. Here, a fluxon is emitted into the right LJJ [Fig. 3(a5)], but in contrast to Fig. 2 it is an *antifluxon* (a fluxon with inverted polarity, $\sigma = -1$).

If the two fluxon polarities $\sigma = \pm 1$ encode the bit states 0 and 1, these unconventional fluxon scattering phenomena implement one-bit reversible gates. The process of Fig. 2 (Fig. 3) performs an ID (NOT) operation by preserving (inverting) the polarity of the input fluxon, during which only 2.1% (2.6%) of the initial fluxon energy $E_{\text{fl}} = 10E_0$ is dissipated. This results in a dissipation $< 0.03E_{\text{fl}} \ll U_{\text{fl}} = 8E_0$, much less than the potential energy (rest energy) of the fluxon U_{fl} .

The small energy difference between the input fluxon and the output fluxon is dissipated in the form of plasma waves generated at the interface and radiated into the LJJs (see the faint wave patterns in Figs. 2 and 3). In addition to this loss

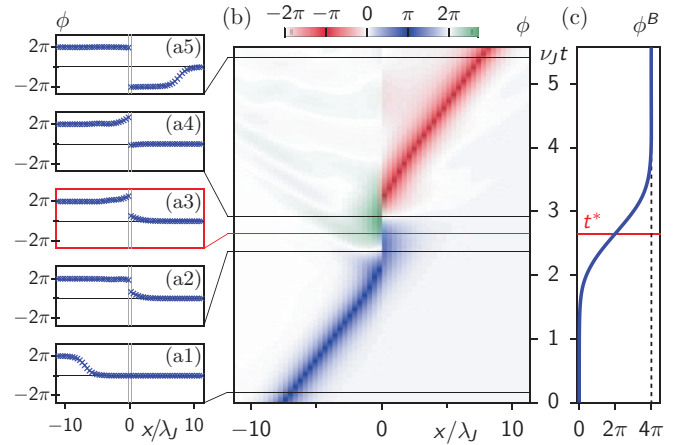


FIG. 3. Polarity-inversion (NOT) gate realized with one-bit gate structure. Subfigures and parameters as in Fig. 2, except for $C_J^B/C_J = 12.0$. In (b) the blue color of the fluxon trace at $x < 0$ and red color at $x > 0$ indicate a conversion from fluxon to antifluxon. Even though the center junction has wound by 4π , the interface stores no flux before or after the gate.

mechanism, we expect smaller losses from (superconductor) quasiparticles and dielectric loss; methods to control these mechanisms are known, even in qubits where the sensitivity is much higher to loss than our gates.

The interface parameters of Figs. 2 and 3 were chosen near numerically optimized values for the two respective gate types. The optimization studies are presented in Sec. IV. As described above, a conversion between the two gate types is here accomplished by adjusting the capacitance C_J^B alone. Another parameter change has a similar effect, namely, an increased I_c^B can turn an ID into a NOT [compare Fig. 7(c2)]. It is important to emphasize that each gate by itself is fully autonomous, requiring no drive fields, and is determined by the fixed circuit parameters alone. The efficient gate dynamics takes place on the timescale of the inverse plasma frequency $2\pi/\omega_J$.

These one-bit gates operate with one fluxon (bit) at a time. Therefore, the spacing required between fluxons must be greater than the sum of two terms. The first term is to avoid perturbations of the gate dynamics by a second arriving fluxon, and is given by the gate time multiplied by the velocity. The second term is related to possible interactions between consecutive fluxons because of their finite width. For our intended velocity ($v \sim 0.6c$), this width is $\gtrsim \lambda_J$.

The fluxon gates differ fundamentally from existing reversible logic where adiabatic drive fields [9,10] slowly evolve the gate potential while at all times retaining the state close to the potential minimum [8]. The fluxon gates also contrast conventional SFQ gates which dissipate the potential energy during damped switching from the high-energy state to the low-energy state.

C. Collective coordinate model

To understand these complex nearly ideal elastic dynamics, we employ a collective coordinate (CC) approach [24]. Here, we briefly sketch the method and start the analysis of the

one-bit gates above. More detail on the CC approach will be provided in Sec. III.

As an ansatz for the fields in left and right halves of the circuit we choose

$$\begin{aligned}\phi(x < 0) &= \phi^{(\sigma, X_L)}(x) + \phi^{(-\sigma, -X_L)}(x) - 2\pi(1 - \sigma), \\ \phi(x > 0) &= \phi^{(-\sigma, X_R)}(x) + \phi^{(\sigma, -X_R)}(x) - 2\pi,\end{aligned}\quad (5)$$

each consisting of a linear superposition of fluxon and mirror antifluxon fields, where $\phi^{(\sigma, X)}$ is defined in Eq. (3). This conveniently parametrizes the possible asymptotic behavior of elastic scattering for our interest: for one incident fluxon of polarity σ [see insets of Fig. 7(a)]. Asymptotically, if the coordinate X_i ($i = L, R$) is far away from the interface, the field in the LJJ i , as defined in Eq. (5), can be either fluxonlike or antifluxonlike, and we refer to it as a particle. We note that, even though the coordinate X_L (X_R) can assume any value in $(-\infty, \infty)$, the left (right) particle energy is always localized within the real space of the left (right) LJJ, about $x_{qL} \simeq -|X_L| \leq 0$ ($x_{qR} \simeq |X_R| \geq 0$). For $X_i = 0$, the particle excitation vanishes. For example, an incident fluxon in the left LJJ is represented by $X_L \ll -W$, $X_R = 0$. Also, a fluxon (antifluxon) in the right LJJ is given by $X_L = 0$ and $X_R \gg W$ ($X_R \ll -W$). From fits to the numerical solutions $\phi_n(t)$ we find that Eq. (5) for $|X_{L,R}| \lesssim W$ also approximates the observed large interface oscillation [around the state $\phi(x) = 2\pi\Theta(-x)$] during gate dynamics.

By inserting ansatz (5) in the system Lagrangian (1), the many degrees of freedom reduce to the two collective coordinates $X_{L,R}$. Using justifications above, we also constrain $\phi^B - \phi_L + \phi_R = 0$ in the CC calculations, thereby eliminating the interface phase ϕ^B . This approximation is valid in a leading-order perturbation expansion of the interface equations of motion, due to the small interface inductance $\hat{L} \ll L\lambda_J^2/a^2$, as fulfilled in the simulations of Figs. 2 and 3. We then obtain coupled equations of motion

$$\begin{pmatrix} \ddot{X}_L \\ \ddot{X}_R \end{pmatrix} = -\mathbf{M}^{-1} \begin{pmatrix} c^2 \frac{\partial U}{\partial X_L} + \frac{1}{2} \frac{\partial m_L}{\partial X_L} \dot{X}_L^2 + \frac{\partial m_{LR}}{\partial X_R} \dot{X}_R^2 \\ c^2 \frac{\partial U}{\partial X_R} + \frac{1}{2} \frac{\partial m_R}{\partial X_R} \dot{X}_R^2 + \frac{\partial m_{LR}}{\partial X_L} \dot{X}_L^2 \end{pmatrix}, \quad (6)$$

where the mass matrix \mathbf{M} is given in Sec. III. The diagonal mass matrix components $m_i(X_i)$ ($i = L, R$), describe the particle mass which varies near the interface ($X_i = 0$). The off-diagonal mass (coupling) components $m_{LR} \propto C_J^B g_I(X_L) g_I(X_R)$ approach zero away from the interface, with $g_I(X_i) = 4(\lambda_J/W) \text{sech}(X_i/W)$. The mass coupling is proportional to the center JJ capacitance C_J^B , and this is a key to coupling between a particle in the left LJJ and the right one.

The potential $U(X_L, X_R)$ is symmetric under the coordinate exchange $X_L \leftrightarrow X_R$ and is of the form

$$U = U_0 + \frac{\hat{I}_c - I_c + I_c^B}{I_c \lambda_J / a} u_1 + \frac{I_c^B}{I_c \lambda_J / a} u_2. \quad (7)$$

Herein, $U_0(X_L, X_R)$ and $u_1(X_L, X_R)$ have even parity under each of the transformations $X_i \leftrightarrow -X_i$ ($i = L, R$), while $u_2(X_L, X_R)$ has no parity symmetry. One potential landscape U is shown in Figs. 4(a) and 4(b). These correspond to the ID and NOT gates of Figs. 2 and 3, respectively, and are identical since both gates have the same critical currents \hat{I}_c and I_c^B . For

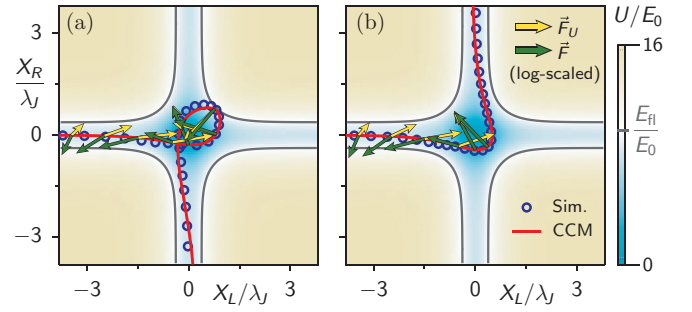


FIG. 4. Trajectories $(X_L, X_R)(t)$ for interfaces of (a) Fig. 2 (ID) and (b) Fig. 3 (NOT). (a), (b) Identical potentials $U(X_L, X_R)$ from Eq. (7). Trajectories obtained from collective coordinate (CC) equations of motion Eq. (6) (red line) and from fit of simulated $\phi_n(t)$ with Eq. (5) (blue marker). Arrows show accelerations (mass-normalized forces) in Eq. (6), \vec{F}_U from the potential (yellow arrows) and the total force $\vec{F} = \vec{F}_U + \vec{F}_M$ (green). Both \vec{F}_U and \vec{F} differ substantially between (a) and (b) even initially, despite still comparable positions $(X_L, X_R)(t)$, e.g., first three arrows near $X_R = 0$ have visibly different arrow lengths despite logarithmic scaling. This is caused by larger mass-matrix elements in (b), where C_J^B is double of (a), and results in stronger initial acceleration in $-X_R$ direction. This causes a larger deflection of the trajectory from $X_R = 0$, as well as a slowed down forward evolution (trajectory points) relative to (a). Within the central potential well accelerations are exponentially larger and dominated by \vec{F}_U .

either of $|X_{L,R}| \gg W$, the potential forms four valleys, each corresponding to a single fluxon as described earlier. A central well exists at $(X_L, X_R) \approx (0, 0)$. Due to $I_c^B, |\hat{I}_c - I_c| \ll I_c$ the interface potentials $u_{1,2}$ contribute only weakly to U , and the valleys are therefore connected with the central well below the initial fluxon energy $E_H/E_0 = 10$ (gray equipotential line). Thus, in principle, conservative scattering between valleys is possible. The gates of Figs. 4(a) and 4(b) differ by *capacitance* and thus mass matrix alone, but have identical CC potential with negligible u_2 contribution. We note, however, that the parity-breaking contribution of u_2 can also be used to change the gate type from ID to NOT. This is done by increasing I_c^B and is discussed in Sec. III.

In Figs. 4(a) and 4(b), the CC trajectories $(X_L, X_R)(t)$ are shown (red lines) for the ID and NOT gates, as obtained from integration of Eq. (6) with initial conditions $X_L = X_0 \ll -W$, $\dot{X}_L = v_0$, and $X_R = \dot{X}_R = 0$. These can be compared with trajectories obtained from accurate fits of the ansatz [Eq. (5)] to the numerical simulation data from Figs. 2 and 3 (blue markers). From the good agreement between the two, we conclude that the CC equations of motion accurately produce the correct forward-scattering dynamics. In Fig. 4(a) the trajectory exhibits a net angular rotation of $3\pi/2$ into the valley with $X_R < 0$, corresponding to a fluxon emitting into the right LJJ (ID gate); in Fig. 4(b), a $(\pi/2)$ rotation of the trajectory into the valley with $X_R > 0$ corresponds to the emission of an antifluxon (NOT gate). The trajectories evolve from initial conditions $X_R = \dot{X}_R = 0$ to $X_R \leq 0$, although no significant potential coupling exists between X_L and X_R due to negligibly small I_c^B . The coupling is instead provided by the coupling mass m_{LR} in Eq. (6), stemming from the relatively large capacitance C_J^B .

In the particle interpretation originating from the ansatz, an incident fluxonlike particle from the left LJJ changes its character at $|X_L| \lesssim W$ and also excites a particle in the right LJJ from $|X_R| \lesssim W$ [see second diagram of Figs. 1(b1) and 1(c1)] as well as panels 1(b2) and 1(c2)]. Finally, the left particle remains at $X_L = 0$, while the right one (initially at $X_R = 0$) exits ($|X_R| \rightarrow \infty$) with fluxonlike or antifluxonlike character [see last diagram of Figs. 1(b1) and 1(c1)]. We will analyze these dynamics in detail in Sec. III C, after giving more detail of the CC (Sec. III A) and discussing general CC dynamics observed for different interface parameters (Sec. III B).

The logic allows a comparison to billiard ball logic [12], which ideally can perform reversible computing gates in two spatial dimensions (2D), using perfect hard collisions with barriers and each other. Standard scattering in a single sine-Gordon (or LJJ) system seems unlikely since there is only a delay from weak interactions between solitons (fluxons) which induces only time delays from ballistic collisions. However, our one-bit fluxon gates introduce elastic collisions at the interfaces due to a strongly coupled interface between the LJJ, which are confined to 1D segments (LJJs). Rather than altering particle paths, as in the billiard ball model, they can change the particle type (polarity) during a collision. The collisions are accurately described by the above particle to particle collision. The excitations of an input particle from $|X_L| \ll W$ interact with the other particle at $X_{L,R} \simeq 0$, and induces scattering to $|X_R| \gg W$.

D. Two-bit gate

We next exploit the different one-bit gate dynamics for the design of a conditional two-bit gate, which depends on the interaction of the fields created by the input fluxons. This gate circuit is shown in Fig. 5(a). It has vertical mirror symmetry as well as mirror symmetry along the propagation direction (left-right). For optimized interface parameters, as given in the caption, near-elastic forward scattering takes place for synchronized input fluxons. Elastic behavior here implies that in both cases, equal and opposite polarity input, nearly all of the energy is returned such that the output velocity nearly equals the input velocity. The output depends on the polarities of the input fluxons: both undergo polarity inversion if they are of the same polarity, as shown in Fig. 5(b), but input fluxons of opposite polarity both retain their original polarities, as shown in Fig. 5(c). When encoding bit states by polarities, this yields a controlled NOT(SWAP) = NSWAP gate: state pairs (0,0) and (1,1) are reversibly converted into each other, while state pairs (0,1) and (1,0) remain invariant. Similar to the one-bit gates, only 2.1% of the initial fluxon energy is dissipated in any of the NSWAP operations. Also, with a change of the interface cell topology, through the use of wiring crossovers, the NSWAP is converted into a SWAP. We note that, even though such two-bit gates could also be obtained by mere rerouting (wiring crossover), the NSWAP gate presented here is fundamentally different since it relies on the strong interaction between the bit states at the interface. This is the first discovered two-bit gate of the fluxon logic type; other two-bit RFL gates have been subsequently investigated [23].

The dependence of the interaction in the interface cell on the relative polarities of the input fields can be understood

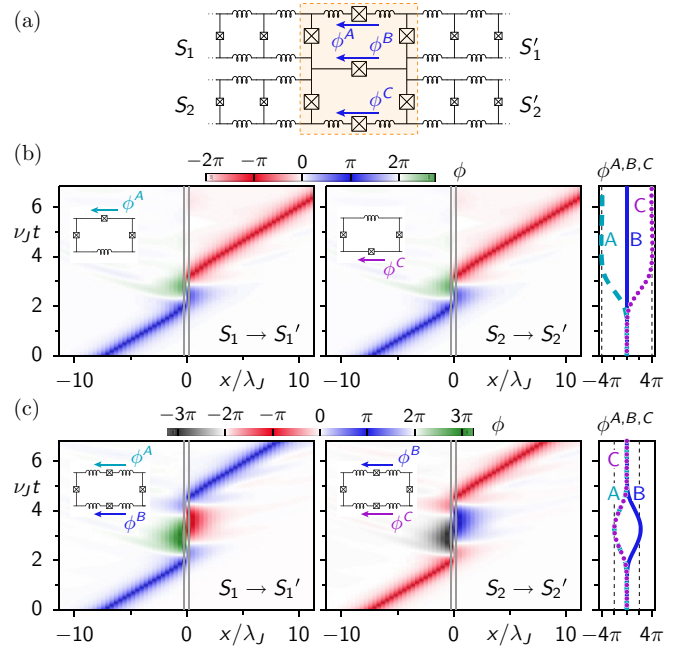


FIG. 5. (a) Schematic of two-bit NSWAP gate connecting input LJJs (S_1 and S_2) and output LJJs (S_1' and S_2'), with left-right and vertical symmetry (the interface in the dashed box has equal A and C junctions). Labeling as in Fig. 2, except here two inductors flank upper and lower interface junctions, each with total inductance $\hat{L}_A = \hat{L}_C$. (b), (c) Color representation of ϕ_n vs x_n and t in LJJ 1 (left) and LJJ 2 (center), and interface phases $\phi^{A,B,C}$ vs t (right), for input fluxons with $v_0 = 0.6c$. For input fluxons with (b) equal polarity the currents across the center-interface JJs (ϕ^B) cancel such that an equivalent one-bit gate [inset and Fig. 10(b)] would have one center JJ. For input fluxons with (c) opposite polarity, the currents across ϕ^B add; an equivalent one-bit gate exists with two center JJs [inset and Fig. 10(c)]. Note that center currents are predominantly through capacitors, e.g., C_j^A and C_j^B . Interface parameters $C_j^A/C_j = 11.2$, $C_j^B/C_j = 22.0$, $\hat{C}_j/C_j = 5.82$, $I_c^A/I_c = 0.02$, $I_c^B/I_c = 0.01$, $\hat{L}_c/I_c = 0.53$, and $\hat{L}^A/L = 0.30$.

from the dynamical equivalence with one-bit gates. We note that the value of \hat{C}_j here is similar to that of the previously presented one-bit gates, which allows comparisons of the top or bottom part of the two-bit gate to the previously discussed one-bit dynamics. If the input fluxons have the *same polarity*, the center-interface current vanishes for symmetry reasons, and the center junction is not excited, $\phi^B = 0$. Here, the dynamics of the upper and lower parts of the interface are thus equivalent [see Fig. 5(b) insets] to two individual one-bit interfaces, each with a center junction equal to the upper center junction (C_j^A , I_c^A) of the two-bit interface in Fig. 5(a). These parameters closely agree with those of the center junction of Fig. 3 and thus the dynamics corresponds to a NOT gate for each input fluxon. On the other hand, if the input fluxons have *opposite polarities*, the interface dynamics in the upper and lower parts are effectively decoupled in another way. In this case, the upper and lower parts of the interface are each dynamically equivalent to a one-bit interface that has two center junctions rather than the one discussed previously [see insets to Fig. 5(c), compare also to Fig. 13]. One of the

equivalent center junctions is the same as the upper center junction of the two-bit interface with values (C_J^A, I_c^A) . The second equivalent center junction must carry half the current of the two-bit interface junction. As a consequence, it must have values $(C_J^B/2, I_c^B/2)$ in order to produce the same phase winding ϕ^B . The critical currents $I_c^{A,B}$ are small such that we neglect them for this discussion. We see from the numerical values of our two-bit gate that $C_J^B/2 \approx C_J^A$ which explains that $\phi^A \approx -\phi^B$ during the dynamics. It is intuitive to see that this can be approximately simplified further to a one-bit interface with one center junction because the two center junctions are in series and thus act as a single interface junction with capacitance $\approx C_J^A/2 \approx 6.1C_J$ (also described in Fig. 10 below). This is in close agreement with Fig. 2, where the center-interface junction has the capacitance $C_J^B = 6.0C_J$. Therefore, as expected from analysis, the ID gate is generated for each of the input fluxons of opposite polarity.

Continuing the comparison with billiard ball logic started above, we see that interactions between fluxons allow them to switch their polarity conditionally, while billiard balls conditionally change their paths due to collisions. Here, the length scale of the interaction is defined by the Josephson penetration depth λ_J . Furthermore, this two-bit gate shares features with one-bit gates, such as large center-interface capacitance which allows the oscillatory dynamics for reversible and nondissipative fluxon gates.

Finally, we have tested the NSWAP gate in a realistic test platform, as shown in Fig. 1(e). Figure 6 shows the results of the simulation. A fluxon is launched by ramping up the external voltages $V_{1,2}(t)$ of transmission lines which are inductively coupled to the input LJJ's. The gate parameters are identical to those in Fig. 5, however, a ground plane is simulated by adding a stray capacitance to ground at each side of a junction, with a value $C_g = 0.05C_J$. The larger phase fluctuations relative to the simulations of Fig. 5 are related to small LJJ dimensions (each LJJ consists of 14 JJs), capacitive coupling to ground (while interface not optimized under this condition), and small imbalance between external voltages [$\max(|V_2|) = 1.06 \max(|V_1|)$]. In this test platform, the output fluxons are stored in loops with large inductance L_t while parallel resistances R_t allow the fluxons to quickly create persistent currents in the storage loops. This test platform simulation shows the same fluxon logic despite nonideal launch conditions (including nonequal waveforms and short left-hand-side LJJ's) and nonoptimized gate (created by added ground plane capacitance).

As the gate examples in Sec. II illustrate, individual logic gates can operate fully ballistic, without external energy supply apart from the input fluxons themselves. In Sec. IV the process margins of the gates will be specified based on a 90% velocity (95% energy) retention after the gate, although a less stringent criterion may be practical. Even for Nb technology, this may allow a ballistic gate with an energy cost on the order $k_B T$ (see below). However, a logic architecture consisting of many individual gates needs to include clocking structures to synchronize fluxons. For example, in simulations of a NSWAP gate we find that the two input fluxons of equal velocity must be spaced by less than $0.4a$ for proper gate operation. In another work [23] we present ‘‘store-and-launch’’ gates which can stop moving fluxons, store the bits as static flux

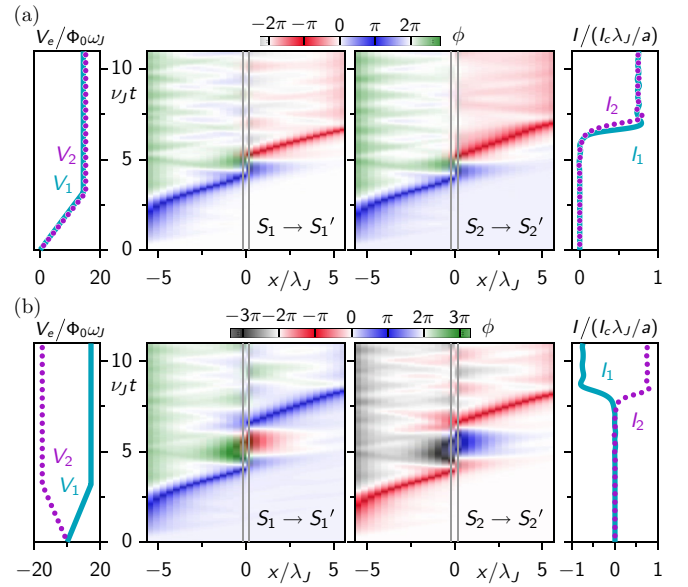


FIG. 6. NSWAP gate dynamics of test platform in Fig. 1(e): external voltages $V_{1,2}(t)$ applied to LJJ's 1 and 2 (left), color representation of ϕ_n vs x_n and t in LJJ 1 (center left) and LJJ 2 (center right), and currents $I_{1,2}$ in storage loops for readout (right), for (a) equal and (b) opposite signs of ramped external voltages. The interface parameters are the same as in Fig. 5. The added phase fluctuations relative to Fig. 5 are primarily related to small LJJ dimensions (each LJJ consists of 14 JJs), capacitive coupling to ground (while interface not optimized under this condition), and small imbalance between external voltages [$\max(|V_2|) = 1.06 \max(|V_1|)$]. The circuit parameters, consistent with Nb fabrication, are $C_J = 125$ fF, $L = 62.8$ pH, $\nu_J = 21.5$ GHz, $\nu_J T_{\text{ramp}} = 3.2$; the TL-LJJ coupling has $L_c = 160$ pH (both TL and LJJ loop) and 20% relative mutual inductance; the storage loops have $L_t = 20L$ and $R_t = \sqrt{L/C_J}$; each LJJ node is coupled to ground with capacitance $C_g = 0.05C_J$.

states, and from these later relaunch fluxons in a synchronized way. In the process of stopping a fluxon, it may conserve the fluxon's potential energy, which makes up 80% of the total fluxon energy (for $v_0/c = 0.6$). In contrast, conventional SFQ logic gates dissipate several units of bit energy, $I_c \Phi_0$, per gate [4,30]. We may compare the fluxon's kinetic energy $E_K = 2E_0$, which is lost when stopping the fluxon and thus forms an upper boundary for the energy loss in a ballistic gate, with the thermal energy $k_B T$: Demanding that the thermal excitation of plasma waves in the LJJ should be suppressed, we require that $k_B T < \hbar\omega_J$, where $\hbar\omega_J = \sqrt{E_C/E_L}E_0$ is the minimum energy of the LJJ plasma spectrum, with $E_L = \Phi_0^2/(8\pi^2L)$ and $E_C = (2e)^2/(2C_J)$. Thus, we see that E_0 should exceed $k_B T \sqrt{E_L/E_C}$, and we can therefore estimate that the (kinetic) energy loss of a fluxon in a stop-and-launch gate may be of the order or larger than $E_K = 2k_B T \sqrt{E_L/E_C}$. For some realistic designs of the discrete LJJ made with Al (Nb) and for a target temperature of 0.5 K (4 K), the factor $\sqrt{E_L/E_C}$ may be on the order 2–50, thus resulting in an energy loss of 4–100 $k_B T$.

III. COLLECTIVE COORDINATE MODEL

In this section we describe more details of the collective coordinate (CC) approach leading to Eq. (6), and employ it to explain elastic scattering phenomena in the circuit interfaces.

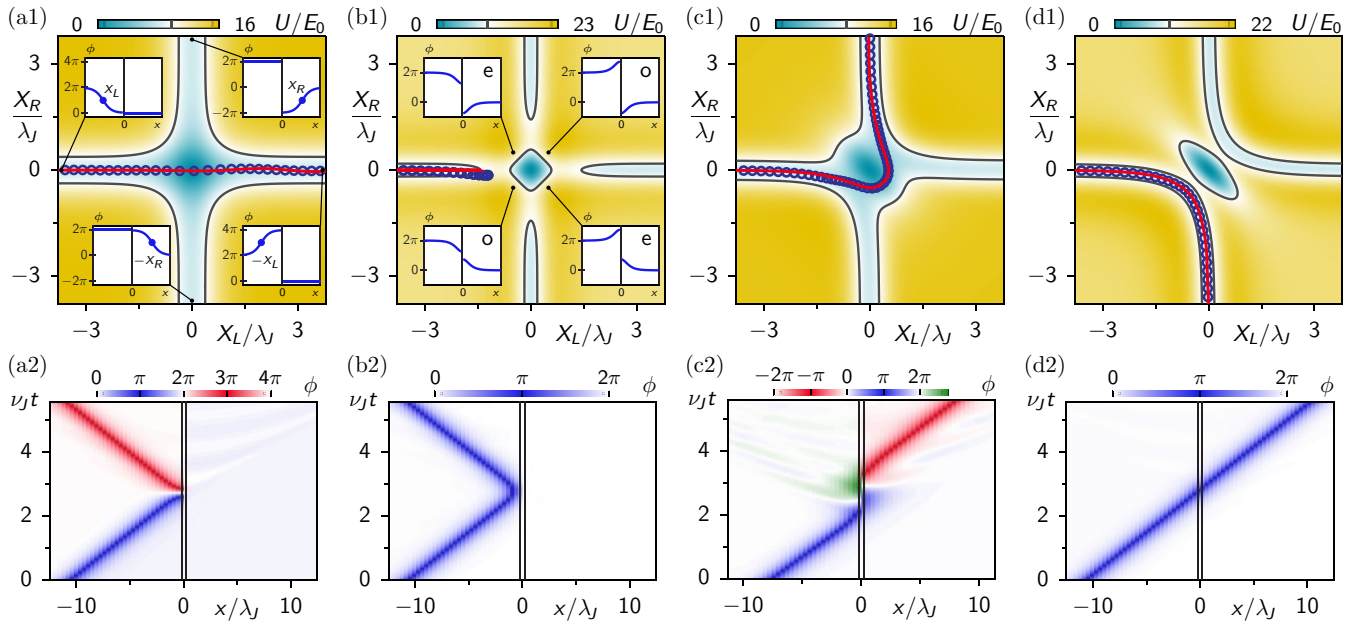


FIG. 7. Elastic scattering cases in one-bit gate structure [Fig. 1(a)], but with interface parameters different from gates. Upper panels: potentials $U(X_L, X_R)$ [Eq. (9)]. Trajectories $(X_L, X_R)(t)$ from reduced (CC) equations of motion [Eq. (13)], shown for initial condition $\dot{X}_L = v_0 = 0.6c$, $X_L \ll -W$, and $X_R = 0$ (red line). Trajectories $(X_L, X_R)(t)$ from fit of simulated $\phi_n(t)$ with Eq. (5) (blue marker). Lower panels: ϕ_n vs x_n and t from simulation for each upper panel. Insets in (a1) and (b1) sketch CC ansatz $\phi(x)$ [Eq. (5)] evaluated at specific points (X_L, X_R) and $\sigma = 1$, e.g., in (a1) clockwise from upper left: input fluxon, transmitted fluxon, reflected antifluxon, and transmitted antifluxon. Interface parameters: (a), (b), (d) $\hat{L}/L = 0.10$, $C_J^B/C_J = 0.10$, $\hat{C}_J/C_J = 1.0$. (a) $I_c^B/I_c = 0$, $\hat{I}_c/I_c = 1.0$. (b) $I_c^B/I_c = 0$, $\hat{I}_c/I_c = 10.0$. (c) $I_c^B/I_c = 2.9$ while all other parameters are the same as in Fig. 2. (d) $I_c^B/I_c = 10.0$, $\hat{I}_c/I_c = 1.0$.

A. Reduced (collective) equations of motion

The starting point of the analysis is the ansatz (5) for the fields in the left and right halves of the circuit shown in Fig. 1(a), each consisting of a superposition of a fluxon and mirror antifluxon. This ansatz is consistent with the initial-state phases far away from the interface, namely, $\phi(x \rightarrow -\infty) = 2\pi$ and $\phi(x \rightarrow \infty) = 0$ for a fluxon incident from the left. As found above, Eq. (5) can be used to approximate $\phi_n(t)$ in the numerically simulated elastic scattering phenomena, e.g., for Figs. 2 and 3. In these fits, $X_{L,R}$ are independent fit parameters for each time t while parameters W and σ were fixed to correspond to the initial fluxon. According to Eq. (5), the symmetry point $(X_L, X_R) = (0, 0)$ corresponds to an equilibrium field $\phi(x) = 2\pi\Theta(-x)$. Localized excitations around this state are described with $|X_{L,R}| \lesssim W$, some of which are sketched in the insets of Fig. 7(b1), in particular even-parity excitations with $X_R = -X_L$ and odd-parity excitations with $X_R = X_L$ (labeled as e and o in the insets). A full set of asymptotic scattering states are parametrized by Eq. (5) as illustrated in the insets of Fig. 7(a1): The fluxon in the left LJJ itself is represented by $X_L \ll -W$, $X_R = 0$. Its reflection as an antifluxon is described by $X_L \gg W$, $X_R = 0$. The forward scattering into fluxon and antifluxon are described with $X_R \ll -W$ and $X_R \gg W$, respectively, with $X_L = 0$.

The following paragraphs summarize results of the CC derivation given in Appendix B 1. The scattering phenomena discussed here occur in a regime of small interface inductance $\hat{L} \ll L\lambda_J^2/a^2$. In this limit, the interface equations of motion allow the approximation $\phi^B \approx \phi_L - \phi_R$. Using this

approximation and the ansatz (5), the Lagrangian (1) can be written in a dimensionless form $\tilde{\mathcal{L}} = \mathcal{L}/E_0$ as

$$\tilde{\mathcal{L}} = \frac{m_L \dot{X}_L^2}{2c^2} + \frac{m_R \dot{X}_R^2}{2c^2} + m_{LR} \frac{\dot{X}_L \dot{X}_R}{c^2} - U(X_L, X_R) \quad (8)$$

with the dimensionless particle potential U :

$$U = U_0 + \frac{\hat{I}_c - I_c + I_c^B}{I_c \lambda_J / a} u_1 + \frac{I_c^B}{I_c \lambda_J / a} u_2. \quad (9)$$

The coordinate-dependent, dimensionless particle masses are

$$m_i(X_i) = m_0(X_i) + \frac{\hat{C}_J - C_J + C_J^B}{C_J \lambda_J / a} (g_i(X_i))^2 \quad (10)$$

($i = L, R$), where $m_0(X_i)$ are the LJJ contributions to the mass, given in Eq. (B7). The interface factor

$$g_i(X_i) = 4(\lambda_J/W) \operatorname{sech}(X_i/W) \quad (11)$$

characterizes the interface contribution to the masses, as well as the coupling mass

$$m_{LR}(X_L, X_R) = \frac{C_J^B}{C_J \lambda_J / a} g_I(X_L) g_I(X_R). \quad (12)$$

The potential $U(X_L, X_R)$ has constituents $U_0(X_L, X_R)$, $u_1(X_L, X_R)$, and $u_2(X_L, X_R)$, which are defined in Eqs. (B6), (B17), and (B18), and are illustrated in Figs. 12(a)–12(c). Recall that the LJJ potential U_0 and the interface contribution u_1 have even parity under the transformations $X_i \leftrightarrow -X_i$, for $i = L, R$, while the interface contribution u_2 has no parity symmetry. All constituents of U are symmetric under the left-right exchange $X_L \leftrightarrow X_R$, as expected.

The Lagrangian (8) generates the coupled equations of motion for $X_{L,R}$

$$(\ddot{X}_L, \ddot{X}_R)/c^2 = \vec{F}_U + \vec{F}_M, \quad (13)$$

which determine the accelerations \ddot{X}_i by the mass-normalized force $\vec{F} = \vec{F}_U + \vec{F}_M$. The separate contributions to this force from the potential U and from the mass gradients are [cf. Eq. (6)]

$$\vec{F}_U = -\mathbf{M}^{-1} \left(\frac{\partial U}{\partial X_L}, \frac{\partial U}{\partial X_R} \right), \quad (14)$$

$$\vec{F}_M = -\mathbf{M}^{-1} \left(\frac{1}{2} \frac{\partial m_L}{\partial X_L} \frac{\dot{X}_L^2}{c^2} + \frac{\partial m_{LR}}{\partial X_R} \frac{\dot{X}_R^2}{c^2}, \frac{1}{2} \frac{\partial m_R}{\partial X_R} \frac{\dot{X}_R^2}{c^2} + \frac{\partial m_{LR}}{\partial X_L} \frac{\dot{X}_L^2}{c^2} \right). \quad (15)$$

The mass matrix \mathbf{M} is composed of the dimensionless elements $M_{ii} = m_i$ and $M_{i,j \neq i} = m_{LR}$ ($i, j = L, R$) given above.

B. General elastic reflection and transmission

The composite potential $U(X_L, X_R)$ is illustrated in Fig. 7(a1) for $\hat{I}_c = I_c$ and $I_c^B = 0$, such that both u_1 and u_2 do not contribute. The potential $U = U_0$ forms four scattering valleys for the asymptotically free fluxons either left or right of the interface (see insets), which are connected by a central potential well at $X_L = X_R = 0$. The accessible coordinate space is limited by the initial fluxon energy $E_{\text{fl}}/E_0 = 10$ (gray equipotential line). Figure 7(a1) also shows the trajectory $(X_L, X_R)(t)$ obtained from integration of Eq. (13) with initial condition $X_L = X_0 \ll -W$, $\dot{X}_L = v_0$, and $X_R = \dot{X}_R = 0$, corresponding to the incident fluxon (red line). It is in excellent agreement with the corresponding trajectory obtained from fitting $\phi_n(t)$ with Eq. (5) (blue markers).

Here, the interface capacitances are $C_J^B \ll C_J$ and $\hat{C}_J = C_J$, such that the coupling m_{LR} is negligible and the acceleration in Eq. (13) remains small in X_R direction. The resulting motion from $X_L < 0$ to $X_L > 0$ corresponds to the fluxon being reflected as antifluxon, as shown in Fig. 7(a2). Note that, in accordance with an earlier remark, the left particle is throughout this process found at a real-space position $x_{qL} \simeq -|X_L| < 0$ within the left LJJ. This scattering is more general than an open LJJ boundary which also generates antifluxon reflection, as a result of the Neumann boundary condition [31] $\phi'(x = x_{\text{boundary}}) = 0$. Unlike that open boundary, here non-negligible current flows through the left interface junction. We note that in this parameter regime a current-phase relation is observed for elastic reflection at the interface which relates to a general integrable boundary condition for the SGE [32], but which is outside the scope of this work.

Keeping $I_c^B = 0$ but raising $\hat{I}_c \gg I_c$ relative to the previous case results in a finite prefactor to the interface potential u_1 and creates a potential barrier at $|X_i| \approx W$ around the center well as shown in Fig. 7(b1) [compare also to u_1 in Fig. 12(b)]. In particular, if $(\hat{I}_c - I_c + I_c^B)u_1/I_c$ is larger than E_{fl}/E_0 , scattering between the valleys is prevented and the incident particle is reflected before entering the central potential well, as shown in Fig. 7(b2). This is similar to the simple case of a fluxon reflection at a shunted end of a LJJ [with the Dirichlet boundary condition [33] $\phi(x = 0) = 0$], in that the particle will remain fluxonlike.

We next consider $I_c^B > 0$ where the contribution of the interface potential u_2 breaks the even potential parities, as shown in Fig. 7(c1). The trajectory coming in at $X_R = 0$ is therefore subject to a relatively strong acceleration component $F_{U,R}$ by which at first it is deflected toward $X_R < 0$, before moving into the valley with $X_R > 0$. Note that here we have additionally set large values of C_J^B, \hat{C}_J , which modify \vec{F}_U , and also provide a strong mass-gradient acceleration \vec{F}_M . Under their combined action, the trajectory eventually evolves smoothly into the valley at $X_R > 0$, corresponding to an antifluxon released into the right LJJ, as shown in Fig. 7(c2). This forms an alternative NOT gate to Fig. 3 [Fig. 4(b)]. In this alternative, only I_c^B differs from the interface parameters of the ID gate in Fig. 2 [Fig. 4(a)], and therefore the altered potential is responsible for turning the ID into a NOT gate. Recall the gates of Fig. 4 differ only by C_J^B , with negligibly small I_c^B , and thus does not make use of this parity-breaking effect.

If I_c^B increases further, the odd-parity contribution in u_2 disconnects the center potential well from the valleys, as shown in Fig. 7(d1). However, the asymptotic valleys of equal-polarity fluxons become simply connected: ($X_L \ll 0, X_R = 0$) with ($X_L = 0, X_R \ll 0$) and ($X_L \gg 0, X_R = 0$) with ($X_L = 0, X_R \gg 0$). The trajectory is confined to a curved valley which corresponds to the direct transmission of the fluxon across the interface, as shown in Fig. 7(d2).

C. Two NOT gate types, made from one ID gate

Finally, in Figs. 4(a) and 4(b) the potential $U(X_L, X_R)$ and trajectories $(X_L, X_R)(t)$ are illustrated for the interface parameters underlying the gates of Figs. 2 and 3. Recall that both cases have the same potential U because the interface parameters I_c^B, \hat{I}_c are identical. The trajectories demonstrate how the unconventional fluxon dynamics of these cases can be attributed to competition between potential and mass-gradient accelerations \vec{F}_U (yellow arrows) and \vec{F}_M , which create the total acceleration $\vec{F} = \vec{F}_U + \vec{F}_M$ (green arrows). Forward scattering of the fluxon requires a deflection of the trajectory, initially at $X_R = 0$, into one of the valleys at $X_R \neq 0$. The gates are based on interfaces with very small I_c^B/I_c , such that the potential U has approximately even parities. Therefore, a non-negligible mass coupling $m_{LR} \propto C_J^B$ in Eq. (13) is required to deviate from $X_R = 0$. First, while approaching the central potential well $X_L \ll -W$, the trajectory is deflected from $X_R = 0$ by the dominant action of \vec{F}_M , as shown by the green \vec{F} arrows which point in a different direction than the yellow \vec{F}_U arrows. In this limit, and for initially $X_R = \dot{X}_R = 0$, we calculate the X_R component of \vec{F}_M as

$$F_{M,R} \approx -\frac{\dot{X}_L^2}{\omega_J^2 W^2} \frac{2 \frac{C_J^B}{C_J \lambda_J / a}}{1 + \frac{\lambda_L}{W} \frac{C_I - C_J + C_J^B}{C_J \lambda_J / a}} e^{X_L/W}. \quad (16)$$

Although exponentially suppressed for $X_L \ll -W$, $F_{M,R}$ initially dominates compared to the other acceleration components, which scale as $|F_{U,R}| \propto e^{3X_L/W}$ and $|F_{U,L}|, |F_{M,L}| \propto e^{2X_L/W}$. $F_{M,R}$ deflects the incoming trajectory toward $X_R < 0$. Then, once it enters the central potential well at $|X_L| < W$, this small deviation $X_R < 0$ experiences a strong restoring force dominated by \vec{F}_U .

In Fig. 4(b) (the NOT gate) the initial deflection is larger than in Fig. 4(a) (the ID gate) due to the larger value of C_J^B . Note that the force arrows in Fig. 4 are scaled logarithmically, such that the initial green acceleration arrow in (b) appears only slightly longer compared to (a), while $F_{M,R}$ in fact is a factor 1.4 larger in (b) according to Eq. (16). The result of larger initial acceleration counteracting the motion in (b) is seen in the lower speed of the particle at $X_L < -W$, as indicated by the smaller separation of the adjacent markers representing the trajectories at equal time steps. The force balance is designed here to symmetrically reflect the trajectory in the potential well at a point on the symmetry line $X_R = -X_L < 0$ (the velocity component along that direction vanishes). The result is a total $(\pi/2)$ counterclockwise rotation into the valley with $X_R > 0$, as described above.

In Fig. 4(a) the initial deflection of the ID gate is reduced by a factor 1.4 due to the half value of C_J^B [see Eq. (16)] relative to Fig. 4(b). The trajectory thus retains larger velocity in the X_L direction when entering the central potential. It is then reflected symmetrically across the symmetry line $X_R = X_L > 0$, related to a $(3\pi/2)$ rotation. In this case $E_{\text{fl}}/E_0 \gtrsim U(X_L(t), X_R(t))$ near the symmetry line and thus the velocity component perpendicular to this line is also small. This results in slower evolution of the phases compared with the NOT gate, and together with the longer trajectory in the central potential well implies a longer gate time of the ID gate.

In contrast to Figs. 4(a) and 4(b), where a conversion from ID to NOT gate is achieved by a change of the interface parameter C_J^B alone, this conversion can also be achieved with a different parameter change, by tuning the interface potentials u_1 and u_2 through I_c^B . This was discussed in Sec. III B, where the increase from $I_c^B/I_c \ll 1$ to $I_c^B/I_c \approx 3$ generates the NOT gate of Fig. 7(c2). The corresponding CC potential and trajectory are shown in Fig. 7(c1). In this example, the initial deflection to $X_R < 0$ is enhanced compared to the ID gate [Fig. 4(a)] by the parity-breaking influence of the interface potential u_2 (other than I_c^B the parameters are the same). Furthermore, the trajectory is slowed down at $X_L \approx -W$ due to a potential barrier introduced by u_1 , such that the trajectory is symmetrically reflected already across the symmetry line $X_R = -X_L < 0$.

IV. GATE OPTIMIZATION AND ROBUSTNESS

The CC analysis based on Eq. (5) was used to explain the role of interface parameters C_J^B , I_c^B , and \hat{I}_c in the dynamics. For example, in the one-bit gates a moderately large capacitance C_J^B is required for the mass coupling $m_{LR} \propto C_J^B$ to generate a non-negligible initial acceleration in the X_R direction $F_{M,R}$, as given by Eq. (16). To achieve gate efficiency beyond the CC predictions, Monte Carlo optimizations were performed, based on the full simulation with Eq. (1), where we vary $C_J^B > C_J$ as an independent variable. For each value of C_J^B we maximize the final velocity v_f of the fluxon emitted into the right LJJ through random iterations of \hat{I}_c , I_c^B , \hat{C}_J , and \hat{L} . Figure 8(a) shows the resulting optimized v_f , obtained with interface parameters presented in Figs. 8(b)–8(e). This is shown for initial velocities $v_0/c = 0.6$ and 0.7 , both for the ID and NOT gates.

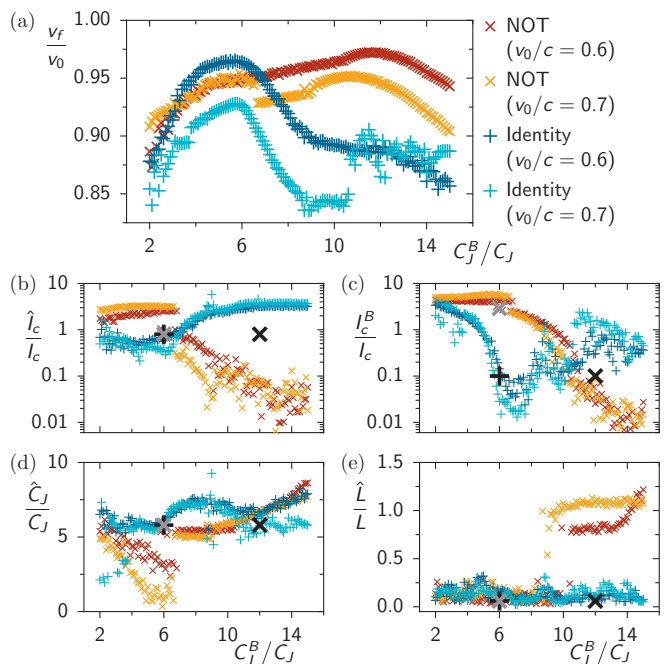


FIG. 8. Interface parameters supporting near-elastic forward scattering for one-bit gates. (a) Final-to-initial velocity ratio v_f/v_0 , for interface with C_J^B and with (b)–(e) values of remaining interface parameters $[\hat{I}_c, I_c^B, \hat{C}_J, \hat{L}]$, obtained from numerical optimization of v_f/v_0 . Optimized parameter sets are shown for NOT gate, with initial velocities $v_0/c = 0.6$ (red \times) and $v_0/c = 0.7$ (orange \times), and for ID gate, with $v_0/c = 0.6$ (blue $+$) and $v_0/c = 0.7$ (light blue $+$). Additional large markers in (b)–(e) indicate gate parameters of ID from Fig. 2 (black $+$), NOT from Fig. 3 (black \times), and NOT from Figs. 7(c1) and 7(c2) (gray \times). Not all parameters need to be close to their optimum for acceptable gate performance, such as \hat{I}_c in the NOT gate of Fig. 3.

For the NOT gate, a broad maximum of $v_f/v_0 \approx 97\%$ is found for $v_0/c = 0.6$ at $C_J^B/C_J \approx 12$, and of $v_f/v_0 \approx 95\%$ for $v_0/c = 0.7$ at $C_J^B/C_J \approx 11$. At even smaller velocities, the maximum is shifted further to higher $C_J^B/C_J > 12$.

The optimized ID gate has a narrower peak in v_f in the displayed range than the NOT gate, with a maximum at $C_J^B/C_J \approx 6$, reaching $v_f/v_0 \approx 97\%$ for $v_0/c = 0.6$ and $\approx 92\%$ for $v_0/c = 0.7$. The optimum C_J^B is less dependent on v_0 for this gate. Around the peaks in v_f , e.g., $C_J^B/C_J \approx 12$ for the NOT gate, the interface parameters are relatively constant, or else are negligibly small:

(i) As shown in Fig. 8(d), for both gates the optimal \hat{C}_J is larger than C_J (as well as C_J^B). It has the approximate value of $\hat{C}_J \approx C_J^B/2$ for the NOT gate (for $C_J^B/C_J > 10$) and $\hat{C}_J \approx C_J^B$ for the ID gate (for $5 < C_J^B/C_J < 8$). In contrast, if \hat{C}_J is strongly reduced from these optimal values, the resulting larger initial deflection toward $X_R < 0$ can destroy the gate dynamics, as understood from the CC analysis [cf. Eq. (16)]. Usually, repeated large-amplitude bounces within the central potential well are then observed. Similar to what happens when C_J^B is increased (as shown in Fig. 4), when \hat{C}_J is reduced from the optimized ID gate of Fig. 4(a) with $\hat{C}_J/C_J = 5.8$ to $\hat{C}_J/C_J = 1$ the initial deflection increases, and as a result the trajectory creates a NOT gate.

(ii) As shown in Figs. 8(b) and 8(c), near the optimization maxima of v_f/v_0 , both I_c^B and \hat{I}_c are small relative to I_c , showing that the short-range interface potentials u_1 , u_2 are irrelevant for the operations of the optimized gates. Instead, these are determined by the balance of mass matrix elements, weighted by C_J^B and \hat{C}_J , in the fixed potential $U \approx U_0$. Only away from their respective optima do the gates increasingly appear to rely on the modification of the potential $U(X_L, X_R)$ by contribution of u_1 and u_2 . This is particularly evident in case of the NOT gate, where I_c^B and \hat{I}_c at $C_J^B/C_J < 6.5$ form an elevated plateau, with $I_c^B, \hat{I}_c > I_c$. For $v_0/c = 0.7$, these parameters even yield a sudden increase of v_f by $\approx 2\%$ to match the performance of $v_0/c = 0.6$ [see Fig. 8(a)]. An example for the dynamics in this regime of large I_c^B and \hat{I}_c [interface parameters indicated by large gray marker in Figs. 8(b)–8(e)] is shown in Figs. 7(c1) and 7(c2). Similarly, for the ID gate away from its optimal C_J^B , \hat{I}_c is enhanced, particularly when $C_J^B/C_J > 8$. This allows u_1 to establish a narrower valley in the X_R direction at $X_L \approx -W$ [see Fig. 12(b)], and this compensates for the larger initial $F_{M,R}$ due to C_J^B in Eq. (16). For $C_J^B/C_J < 4$ (below the optimum) much larger values of I_c^B are observed, and this breaks the even potential parities due to the increased contribution of u_2 . This compensates for the smaller initial $F_{M,R}$ (arising due to smaller C_J^B).

(iii) The Monte Carlo optimization generally yields $\hat{L}/L \approx 0.1$, as shown in Fig. 8(e). This regime is consistent with the assumptions of the CC analysis, which uses $\hat{L}/L \ll \lambda_j^2/a^2$. A seemingly large $\hat{L} \approx L$ is found in plateaus of the NOT gates at $C_J^B/C_J > 10$, but this still corresponds to a small expansion parameter $(\hat{L}a^2)/(L\lambda_j^2) \approx 1/7$, valid in earlier approximations.

The similar parameters for the two gates in Fig. 8 indicate the possibility to convert between the two gate types by adjusting only a single parameter. As examples, we have discussed in Sec. III how the change of either C_J^B from $C_J^B/C_J = 6$ to $C_J^B/C_J = 12$, or of I_c^B from $I_c^B/I_c = 0.1$ to $I_c^B/I_c = 2.9$, can turn a near-optimized ID into a near-optimized NOT gate. The parameters of these three interfaces are indicated in Fig. 8 with the large black and gray markers. As already mentioned, a similar effect can be achieved by decreasing \hat{C}_J .

In Fig. 9 we illustrate the gate robustness with respect to variations in the initial conditions and the interface parameters, for the gates of Figs. 2 and 3. Each panel shows the final velocity of the output fluxons under one of these parameter variations. As demonstrated in Fig. 9(a), the final-to-initial velocity ratio v_f/v_0 as a function of initial velocity v_0 is similar for both ID and NOT gates, yielding $v_f/v_0 > 90\%$ in the wide interval $0.45 \leq v_0/c \lesssim 0.7$. For $v_0/c = 0.6$ this corresponds to an energy loss $\Delta E/E_{\text{fl}} < 5\%$, while optimal forward scattering at the maxima have $\Delta E/E_{\text{fl}} \lesssim 3\%$. The relative insensitivity to the incident velocity is remarkable. Resonant scattering at defects within a LJJ, e.g., local inhomogeneities of I_c or C_J , typically exhibit high sensitivity to velocity variations, as characteristic for chaotic scattering processes [17,18]. We note that our interface cannot directly be compared with a mere LJJ defect: while the latter allows a perturbation treatment within the sine-Gordon theory, our interface involves an essential additional degree of freedom ϕ^B , which allows nonperturbative effects.

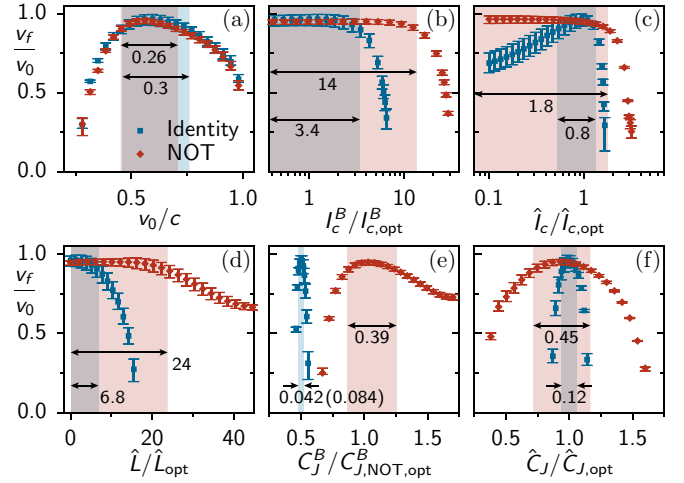


FIG. 9. Robustness of one-bit gates: ratio of gate output to input velocity v_f/v_0 as function of (a) initial velocity v_0 . (b)–(f) Ratio v_f/v_0 for $v_0/c = 0.6$, shown as function of varied interface parameter, which is (b) I_c^B , (c) \hat{I}_c , (d) \hat{L} , (e) C_J^B , and (f) \hat{C}_J . In (a) all interface parameters, and in (b)–(f) all but the varied interface parameter are kept constant at values $\hat{I}_{c,\text{opt}}$, $I_{c,\text{opt}}^B$, \hat{L}_{opt} , $C_{J,\text{opt}}^B$, $\hat{C}_{J,\text{opt}}$, used in Fig. 2 for the ID (blue square) and in Fig. 3 for the NOT gate (red diamond), respectively. Error bars mark the amplitudes of velocity oscillations after scattering. Shaded regions illustrate the ranges wherein $v_f/v_0 > 0.9$. This allows for fast output and a sufficient range of parameters for fabrication. However, only $v_f/v_0 > 0$ is necessary for deterministic (error-free) gate results with potential energy conservation, a minimum requirement for incorporation into a reversible architecture (see text).

The robustness against relative variations p/p_{opt} of one parameter $p \in [I_c^B, \hat{I}_c, \hat{L}, C_J^B, \hat{C}_J]$, with respect to its optimum value p_{opt} , is shown in Figs. 9(b)–9(f). The acceptable range of parameter variations seen in these figures is related to the scatter of optimized parameters in Fig. 8, when the gate parameter [large black marker in Figs. 8(b)–8(e)], lies within the scatter range. The value is in the optimized range within the scatter for the values of \hat{C}_J of both gate types [Fig. 8(d)]. In this case, greater scatter in the parameter is seen in the NOT gate relative to the ID gate, and thus as expected the NOT gate is less sensitive in the \hat{C}_J -gate parameter, as seen in Fig. 9(f). In other cases, the chosen gate parameters lie outside that scatter range because it is not very sensitive to the parameter, such as \hat{I}_c in the NOT gate of Fig. 3. The NOT gate is rather insensitive to most parameter variations, including I_c^B and \hat{I}_c . In line with previous analysis, \hat{L} is small and therefore it is relatively insensitive for both gate types. For the ID gate the criterion $v_f/v_0 \geq 0.9$ gives a large accessible range of $+30\%$ to -48% for parameter \hat{I}_c . It also gives tolerance ranges for C_J^B and \hat{C}_J of 8% and 12% , respectively. Note that the variation of C_J^B is presented in Fig. 9(e) relative to the optimized value of the NOT gate, which is twice that of the ID gate: $C_{J,\text{NOT,opt}}^B/C_{J,\text{ID,opt}}^B = 2.0$. From this analysis, the narrowest tolerance range, 8% in capacitance is for the ID gate, but still shows compatibility with current fabrication processes. Further optimization can be performed, and furthermore the tolerance range (margins) can increase by large factors when setting a lower output-velocity criterion.

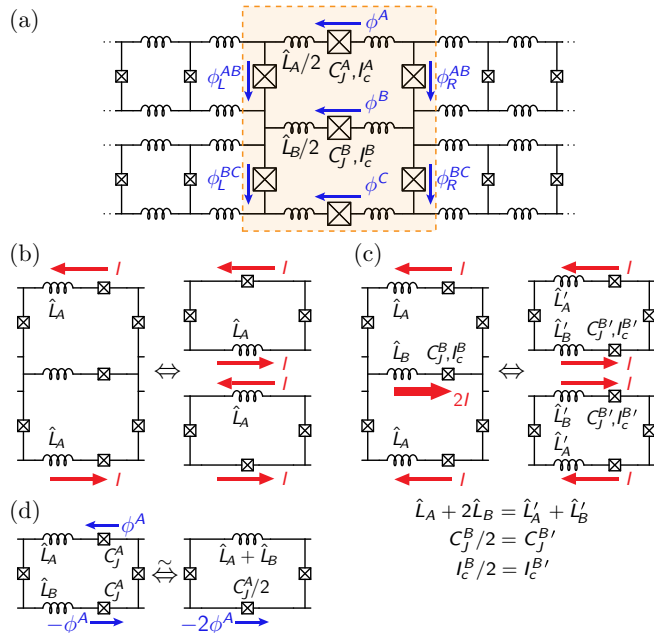


FIG. 10. (a) Two-bit gate with highlighted interface connecting two LJJs from each side. Vertical symmetry ($C_J^C = C_J^A$, $I_c^C = I_c^A$, $\hat{L}_C = \hat{L}_A$, $\hat{C}_J^{BC} = \hat{C}_J^{AB}$, $\hat{I}_c^{BC} = \hat{I}_c^{AB}$) as well as left-right symmetry. Left-right visual symmetry [as in Fig. 1(a)] is shown for $\hat{L}_{A,B,C}$ but later panels combine the two half-sized inductors for an equivalent circuit. Dynamically equivalent one-bit interfaces for input of two synchronized fluxons in the two-bit circuit with (b) equal or (c) opposite polarity. (d) Approximate equivalence between one-bit interfaces, valid for small critical currents $I_c^A, I_c^B \ll I_c$. Labels for invariant parameters in mappings (b)–(d) are omitted.

V. TWO-BIT GATE

Now, we discuss the interface for the two-bit gate [Fig. 10(a)], which connects two LJJs from each side. It is designed as a generalization of the one-bit gate interface, in that it is symmetric in propagation direction (left-right), with central junctions in the interface, labeled A , B , C . We also restrict the circuit to the case of vertical symmetry about the B line, e.g., $C_J^C = C_J^A$. We introduce the notation ϕ^{AB} and ϕ^{BC} for the phases across the junctions in the upper and lower LJJs, respectively.

We discuss here the cases of aligned and antialigned input fields: $\phi_n^{BC} = \phi_n^{AB}$ and $\phi_n^{BC} = -\phi_n^{AB}$, respectively. For synchronized input fluxons of identical velocity the former corresponds to both having equal polarities, and the latter to opposite polarities. A coupling between fields of upper and lower LJJ can only occur within the interface. The dynamics in the circuit of Fig. 10 cannot be mapped (impedance matched) to dynamics in one-bit interfaces for arbitrary input fields due to the nonlinear circuit elements. However, as detailed in Appendix C, it is possible for the above special initial conditions where the dynamics becomes fully equivalent to the independent evolution in one-bit circuits, such that the initial property $\phi_n^{BC} = \pm\phi_n^{AB}$ remains preserved. For simplicity, we argue in the limit of small interface inductances \hat{L}_A, \hat{L}_C . Similar to the first-order approximation in the CC analysis of Sec. III A, this allows us to employ the interface-

cell constraints $\phi^A - \phi^B = \phi_R^{AB} - \phi_L^{AB}$ and $\phi^B - \phi^C = \phi_R^{BC} - \phi_L^{BC}$. Next, we schematically summarize the formal analysis provided in Appendix C for the two initial cases.

Case I, equal polarities. Here $\phi^{BC} = \phi^{AB}$ and $\dot{\phi}^{BC} = \dot{\phi}^{AB}$. The above cell constraints then imply that $\phi^A - 2\phi^B + \phi^C = 0$. This input symmetry together with the device symmetry imply $\phi^C = -\phi^A$, and thus $\phi^B = 0$. The current in the junction with ϕ^B thus vanishes, while the currents in the junctions with ϕ^A and ϕ^C are opposite. Under these conditions, the interface Lagrangian becomes a sum of two independent contributions, and it is therefore clear that ϕ^{AB} and ϕ^{BC} evolve independently. Because of the vertical interface symmetry, the initial relations $\phi_n^{AB} = \phi_n^{BC}$ then remain fulfilled for all times t . Each of the two independent Lagrangians [Eq. (C5)] turns out to be identical to that of an equivalent one-bit interface [Eq. (B4)], whose center junction equals the A -line junction of the two-bit interface (C_J^A, I_c^A), and whose interface inductance \hat{L} likewise is determined by the A -line inductance \hat{L}_A . This equivalence is illustrated in Fig. 10(b).

Case II, opposite polarities. Here $\phi^{BC} = -\phi^{AB}$ and $\dot{\phi}^{BC} = -\dot{\phi}^{AB}$. The cell constraints then imply that $\phi^A = \phi^C$. The currents in the junctions with ϕ^A and ϕ^C are equal and their sum is compensated by the current in the B line. Again, the interface Lagrangian becomes a sum of two independent contributions Eq. (C6), and each of them is identical to that of an equivalent one-bit interface [compare Eq. (B19)]. This equivalence is shown in the schematics of Fig. 10(c). However, compared with the one-bit interface discussed in the previous case, this one has center junctions both in the A and the B line (cf. Fig. 13). In this equivalent one-bit interface the A -line junction is identical to the original A -line junction of the two-bit interface, with (C_J^A, I_c^A). In contrast, the B -line junction has only half of the original capacitance and critical current ($C_J^B/2, I_c^B/2$). As a result, its junction phase ϕ^B is identical to that in the two-bit interface, while it carries only half of the current $-I = (\Phi_0/2\pi)(C_J^B/2)\dot{\phi}^B + (I_c^B/2)\sin\phi^B$. The sum of inductances in the equivalent one-bit interface equals the sum ($\hat{L}_A + 2\hat{L}_B$) of the two-bit interface. Furthermore, if the equivalent one-bit interface itself has vertical symmetry, i.e., if $C_J^A \approx C_J^B/2$ and if the critical currents $I_c^A, I_c^B/2$ are negligible, then $\phi^B \approx -\phi^A$ in the equivalent one-bit interface with two center junctions. The dynamics becomes approximately equivalent to that in a one-bit interface with only one interface junction, which thus has the equivalent serial capacitance $C_J^A/2$, as shown in Fig. 10(d). See Appendix B 2 for a detailed discussion including CC analysis of the new one-bit interface. The CC analysis can also be extended to model other two-bit gates, if asymmetry prevents a mapping to the two dynamically decoupled one-bit gates.

In summary, these mappings to one-bit circuits imply that synchronized fluxons in two-bit circuits can be made to undergo the forward scattering of one-bit gates. Moreover, as the mappings are different for equal and opposite polarities of the input fluxons, a two-bit gate can be designed which deterministically carries out the NOT or ID processes as a controlled gate. An example for this is the controlled NOT SWAP (NSWAP) gate, described above and in Fig. 5 for a two-bit circuit (with interface parameters $C_J^A/C_J = 12.2$, $C_J^B/C_J = 22.0$, $\hat{C}_J/C_J = 5.82$, $I_c^A/I_c = 0.02$, $I_c^B/I_c = 0.01$, $\hat{I}_c/I_c = 0.53$, $\hat{L}^A/L = 0.30$, and $\hat{L}^B/L = 0$). For equal

polarity fluxons, the equivalent one-bit interface has, according to the mapping of Fig. 10(b), the inductance $\hat{L} = 0.30L$ and capacitances $C_J^A = 12.2C_J$ and $\hat{C}_J = 5.82C_J$, while the critical current of the interface junction is negligible, $I_c^A \ll I_c$. Comparing this to the one-bit gate-optimization curves in Fig. 8 (with line index B instead of A) it is clear that these parameters support a NOT gate, individually executed on both input fluxons. Thus, the input bit-state pairs (0,0) and (1,1) are transformed to output state pairs (1,1) and (0,0), respectively. For opposite polarity fluxons, the equivalent one-bit interface has, according to the mapping of Fig. 10(c), a B junction with capacitance $C_J^B/2 = 11.0C_J$, while all other interface capacitances are invariant, $C_J^A = 12.2C_J$ and $\hat{C}_J = 5.82C_J$. When we simulate the fluxon dynamics for this equivalent interface, using the interface Lagrangian for two center junctions, Eq. (B19) instead of Eq. (B4) for one center junction, we observe forward scattering without polarity inversion, similar to Fig. 2. Because this one-bit interface has approximate vertical symmetry, $C_J^A \approx C_J^B/2$ and negligible $I_c^{A,B}$, we can further compare it with an (approximately) equivalent one-bit interface with only one center junction of serial capacitance $C_J^A/2 \approx 6.1C_J$, as illustrated in Fig. 10(d). Again, from Fig. 8 it is clear that this interface supports an ID gate. For the one-bit interface, this means that the synchronized fluxons here both perform an ID gate, such that input state pairs (0,1) and (1,0) are preserved. The combination of the two input cases creates a NSWAP gate, a gate that depends on the strong interaction of the input fields.

VI. SUMMARY AND CONCLUSION

We have proposed reversible fluxon logic (RFL) as new reversible logic gate circuits. The bit states are represented by the fluxon and antifluxon states in a long Josephson junction (LJJ) which have opposite topological charge (flux polarity). The RFL gates are built from LJJ segments and a circuit interface between them. The key physical feature of the gates is the resonant nonlinear dynamics induced by the incoming fluxon at the interface. We find through numerical circuit simulations that the fluxon is converted at the interface to and then from a localized oscillation mode, thus realizing a forward scattering of the fluxon from one LJJ to the other. Both the moving fluxon and the localized interface mode have a finite width on the order of the Josephson penetration length λ_J , and this facilitates the resonant conversion between these two excitation types. This mechanism therefore distinguishes RFL gates from lumped-element circuits used in SFQ-based (reversible) logic.

Importantly, in the process of forward scattering at the interface the fluxons can undergo conditional changes of their polarity. This effect provides the means of bit switching in the RFL gates. The bit switching is characterized by a 4π change of a central JJ in the gate interface (see Fig. 1), contrasting the 2π switching of strongly damped JJs in SFQ digital logic. The dynamics in the RFL gate circuits is powered only by the inertia of incident fluxons, which distinguishes them from previous reversible digital circuits which use power from an adiabatic clock for dynamics. At the same time, while being a ballistic type of reversible logic, RFL also differs from the classic billiard ball model in that the digital state is not

encoded in the particle paths but their topological charge (flux polarity). Contrary to the billiard ball scattering-based gates in 2D, no path correction is therefore needed in RFL gates since given 1D paths are defined by the LJJs for the result.

As shown in Fig. 9, the scattering process at the interface depends on the circuit parameters and (weakly) on the input velocity of the fluxons. RFL gates are defined with those interface parameters which enable the desired scattering type for fluxons at a moderately high input velocity (e.g., $v = 0.6c$), with a high-energy retention of the output fluxons.

The fundamental building blocks of the logic are the one-bit gate circuits which we design with large shunt capacitances of the three interface JJs (Fig. 1). These capacitances absorb and later release a large fraction of the incoming fluxon's energy. This process is aided by the evanescent field that is excited around the interface over the Josephson penetration length λ_J . Depending on the interface parameters, the new fluxon has inverted or unchanged polarity, and the two circuits therefore define the NOT and identity (ID) gates, respectively. We note that the NOT and ID gate parameters are not unique; a NOT gate may be obtained from an ID gate by modifying the critical current or capacitance in the interface-center JJ. For example, we showed different NOT gates in Figs. 3 and 7 related to the ID gate of Fig. 2.

As there is no external power supply during the gate operation, the energy cost of an RFL gate is given simply by the energy difference between the output and the input fluxons. The fluxon output velocity and energy is calculated for various gate parameters (see Fig. 8). In our simulations with particular gate parameters, the output fluxons recover $>97\%$ of the input fluxon energy, which is $E_{\text{fl}} = 10E_0 = 10\Phi_0 I_c \lambda_J / (2\pi a)$ at a speed $v = 0.6c$.

In a digital architecture consisting of many RFL gates, of course additional structures are required where fluxons are synchronized and brought back to their nominal speed. Even if fluxons are stopped in such components, the entire potential energy of fluxons could be conserved (i.e., their rest mass which is 80% in our study). In later work [23], we describe a circuit structure that allows one to store and launch fluxons for synchronization before entering a ballistic gate. The energy for accelerating the stored fluxons in that structure is supplied by a clock fluxon with low energy relative to the data fluxon.

The operation time of the here presented RFL gates is only a few Josephson oscillation periods $1/\nu_J$ such that the gates are fast as well as efficient. Compared with this, the gate cycle in adiabatically powered reversible gates uses many oscillation periods of a JJ for the operation time in order to meet the adiabatic criteria, to conserve most of the digital state energy $\sim I_c \Phi_0$.

A two-bit NSWAP gate was studied as a natural extension of the one-bit gates. It exhibits (see Fig. 5) one of two types of dynamics, depending on whether the input fluxon polarities are the same or different. For all possible input polarities, a dynamically equivalent one-bit gate can be found, i.e., the coupled dynamics of the two-bit gate is in each case mapped (see Fig. 10) to that of two uncoupled one-bit gates. The two-bit NSWAP was also numerically simulated (see Fig. 6) in a proposed experimental test platform [see Fig. 1(e)] which features capacitive coupling to a ground plane and an imperfect fluxon launch. This simulation shows that the gate

operation is robust even in the presence of nonoptimized stray capacitance and launch-induced plasma waves that perturb the gate dynamics. Simulations of one-bit gates were made over a range of parameters, and the output velocity shows that gates are compatible with current fabrication uncertainties (see Fig. 9).

To explain the numerically discovered phenomena of fluxon conversion to resonant excitation, followed by fluxon (or antifluxon) creation we developed and analyzed a collective coordinate model. In this model, we parametrize the fields in each LJJ as a superposition of fluxon and mirror antifluxon and thus reduce the many-junction dynamics to that of only two coupled coordinates. We solve the resulting reduced system and find quantitative agreement with the solution of the numerical circuit simulation (see Fig. 4). The model describes motion of fluxons and antifluxons in the LJJ as motion in four valleys of a two-dimensional potential which may also be connected to allow scattering between valleys. The energy-conserving scattering process is described not by fluxons, but as particles that change between fluxon and antifluxon types smoothly in time. The influence of kinetic coupling and mass gradients stemming from the interface are essential to the gate dynamics since there is no external modulation of the potential.

Reversible logic is now successfully realized in recent demonstrations of circuits that commonly share an adiabatic drive to steer the dynamics. However, we find that reversible gates are possible with an unrealized type known as ballistic reversible gates. Our collective coordinate model for one-bit gates describes the gate dynamics in terms of particles moving in a static potential under the influence of mass-gradient forces. We expect future experimental studies of these gates for scientific and technological purposes. We also provided estimates for energy limitations related to timing and launching a fluxon, as low as the order of $k_B T$, when used in a future possible architecture.

This provides an efficiency benefit over irreversible gates by orders of magnitude. Also, the addition of ballistic gates enhances the breadth of reversible digital logic. This may ultimately be useful to speed development in reversible digital logic similar to the way a broad set of superconducting qubit types advanced quantum reversible logic.

ACKNOWLEDGMENTS

K.D.O. and W.W. acknowledge useful discussions with Q. Herr, V. Semenov, F. Gaitan, and R. Ruskov. W.W. acknowledges support from University Technical Services.

APPENDIX A: FLUXON RADIATION IN A DISCRETE LJJ

The fluxon in an ideal continuous LJJ can move without energy loss, as described by the soliton solution to the sine-Gordon equation. In a discrete LJJ, as described by the Frenkel-Kontorova model [26], the discreteness acts as a perturbation to the sine-Gordon dynamics. This perturbation causes a coupling between the fluxon and the spectrum of linear plasma waves. As a result, a moving fluxon excites plasma waves and loses energy in a resonant process known as Cherenkov radiation [26,27]. For small to moderate

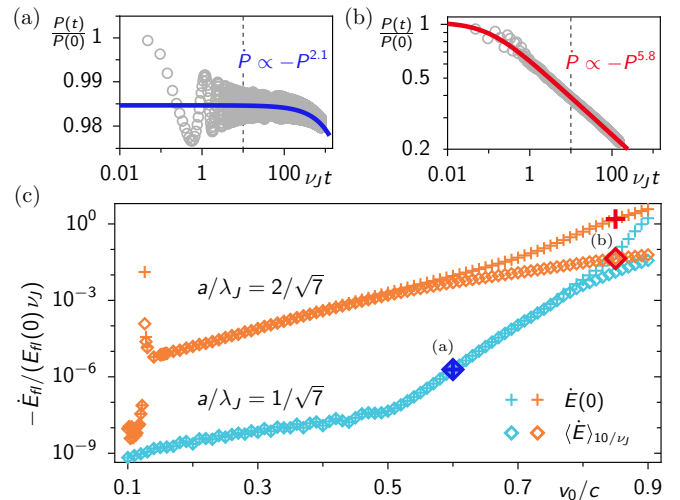


FIG. 11. (a), (b) Simulated momentum evolution $P(t)$ vs t (marker) and fits with Eq. (A2) (solid line), for fluxons initialized with (a) $v_0/c = 0.6$ at $a/\lambda_J = 1/\sqrt{7}$ and (b) with $v_0/c = 0.85$ at $a/\lambda_J = 2/\sqrt{7}$. (c) Dissipation rate \dot{E}_f of the fluxon energy vs initial velocity v_0 for $a/\lambda = 1/\sqrt{7}$ (light blue) and $a/\lambda = 2/\sqrt{7}$ (orange). The time-dependent dissipation rate $\dot{E}_f(t)$ [Eq. (A4)] is calculated from fits of momentum $P(t)$ with Eq. (A2), as in examples (a) and (b). Special markers correspond to $P(t)$ shown in (a) and (b). We show the initial rate $\dot{E}_f(t=0)$ (plus), using $P(0)$ and $\dot{P}(0)$ from Eq. (A2), and the average rate $\langle \dot{E} \rangle$ over time $v_f t = 10$ (diamond); this averaging interval is indicated by the dashed line in (a) and (b).

discreteness, such as the one used in this work, this process is inefficient, whereas at large discreteness the energy loss due to Cherenkov radiation becomes strong [28].

Here, we simulate fluxon motion in our discrete LJJ to show different damping regimes. The dissipation rate of the fluxon energy \dot{E}_f is strongest at ultrarelativistic speeds $v_0/c \rightarrow 1$, and decreases by many orders of magnitude for moderate values of v_0 [see $v_0/c = 0.9$ versus 0.6 in Fig. 11(c)]. For fixed value of v_0 below the ultrarelativistic regime (such as $v_0/c = 0.6$), the dissipation rate also drops by orders of magnitude when the effective lattice spacing a/λ_J is decreased. For example, in Fig. 11 we compare dissipation rates for our default value $a/\lambda_J = 1/\sqrt{7}$ (light blue), with the doubled value $a/\lambda_J = 2/\sqrt{7}$ (orange). At a velocity $v_0/c = 0.6$ the dissipation rate of the latter is $|\dot{E}_f|/E_f \approx 10^{-3}\omega_J$ which may not be negligible, e.g., on a timescale of some $100\omega_J^{-1}$. Compared to that, the dissipation rate for the default discreteness is reduced by orders of magnitude, $|\dot{E}_f|/E_f \approx 3 \times 10^{-7}\omega_J$, and is negligible in the context of this study of gate times on the order of ω_J^{-1} .

The dissipation rate \dot{E}_f presented in Fig. 11 is calculated from the time-dependent fluxon momentum

$$P = 8\dot{X}(E_0/c^2)(1 - (\dot{X}/c)^2)^{-1/2}, \quad (\text{A1})$$

where the velocity \dot{X} follows from the fits of the moving fluxon according to Eq. (3) with fit parameters X and W . As above, we use the characteristic energy $E_0 = (\Phi_0/2\pi)I_c\lambda_J/a$ of the continuum equation, and the characteristic momentum

is E_0/c . We then fit P vs time t with the function

$$P(t) = \frac{\bar{P}}{(1 + \gamma(\alpha - 1)\omega_J t (\bar{P}c/E_0)^{\alpha-1})^{1/(\alpha-1)}}, \quad (\text{A2})$$

where \bar{P} , γ , α are independent fit parameters. This equation follows from a momentum-decay rate proportional to a power $\alpha \geq 1$ of the momentum,

$$\omega_J^{-1} \dot{P} = -\gamma P^\alpha (c/E_0)^{\alpha-1}. \quad (\text{A3})$$

We find that this function describes the momentum decay well over a large range of damping rates, as demonstrated in Figs. 11(a) and 11(b). For very small damping rates, exponential behavior is recovered, $P(t) = \bar{P} \exp(-\gamma\omega_J t)$, corresponding to momentum-proportional damping $\omega_J^{-1} \dot{P} = -\gamma P$ from initial momentum \bar{P} .

Finally, we evaluate the energy dissipation rate

$$\dot{E}_{\text{fl}}(t) = \frac{\dot{P} P c^2}{8E_0} \left(1 + \frac{(cP)^2}{8E_0^2} \right)^{-1/2}, \quad (\text{A4})$$

following from the momentum-energy relation $E_{\text{fl}} = 8E_0[1 + (cP)^2/(8E_0^2)]^{1/2}$ and using $P(t)$ from the momentum fit, Eq. (A2). In Fig. 11(c) we present both the initial dissipation rate from the fit, $\dot{E}_{\text{fl}}(t=0)$ (plus), as well as the dissipation rate $\langle \dot{E} \rangle$ averaged over a time $\omega_J t = 50$ (diamonds), for two discretenesses as a function of the initial velocity v_0 . At large v_0/c the initial decay rate is much higher than the time-averaged one, showing that the dissipation changes rapidly during the averaging time. This is shown in Fig. 11(c), e.g., at $v_0/c = 0.85$, indicated by the (b) markers for the discreteness $a/\lambda = 2/\sqrt{7}$, and the time-dependent momentum for this initial velocity and discreteness is shown in Fig. 11(b). The initial momentum decay rate of Eq. (A3) is large, $\dot{P} \approx -4(E_0\omega_J/c)$ at $t = 0$, and creates a large initial dissipation rate \dot{E}_{fl} . As $\dot{E}_{\text{fl}}(t)$ decays quickly in time, $\langle \dot{E} \rangle$ is much smaller in comparison. At lower velocity and higher discreteness, the energy loss rate is much lower. For example, at $v_0/c = 0.6$ and $a/\lambda = 1/\sqrt{7}$ [(a) markers in Fig. 11(c) with the corresponding time-dependent momentum shown in Fig. 11(a)], $\dot{P} \approx -10^{-5}(E_0\omega_J/c)$ is very small at $t = 0$, and therefore both measures coincide.

The sudden reduction of the dissipation rate observed below $v_0/c \approx 0.12$ for the higher discreteness $a/\lambda_J = 2/\sqrt{7}$ is related to the resonant emission of plasma waves at specific frequencies [28]. Once the fluxon velocity falls below this critical value, an individual solution of the resonance condition becomes inaccessible. As a result, emission into that mode is suppressed.

APPENDIX B: COLLECTIVE COORDINATE ANALYSIS

1. Interface with one center junction (1-JJ)

Here, we present the CC analysis leading to Eqs. (8)–(15), for the circuit of Fig. 1(a). We separate the Lagrangian in Eq. (1) as

$$\mathcal{L} = \tilde{\mathcal{L}}E_0 = (\tilde{\mathcal{L}}_l + \tilde{\mathcal{L}}_r + \tilde{\mathcal{L}}_i)E_0, \quad (\text{B1})$$

where the contributions of left and right LJJ and of the interface are

$$\tilde{\mathcal{L}}_l = \frac{a}{\lambda_J} \sum_{n=1}^{N_l} \left[\frac{1}{2} \frac{\dot{\phi}_n^2}{\omega_J^2} + \cos \phi_n - \frac{(\phi_{n+1} - \phi_n)^2}{2(a/\lambda_J)^2} \right], \quad (\text{B2})$$

$$\tilde{\mathcal{L}}_r = \frac{a}{\lambda_J} \sum_{n=N_l+1}^N \left[\frac{1}{2} \frac{\dot{\phi}_n^2}{\omega_J^2} + \cos \phi_n - \frac{(\phi_n - \phi_{n-1})^2}{2(a/\lambda_J)^2} \right], \quad (\text{B3})$$

$$\begin{aligned} \tilde{\mathcal{L}}_i = & \frac{a}{\lambda_J} \left\{ \frac{1}{2} \frac{\hat{C}_J - C_J}{C_J \omega_J^2} [\dot{\phi}_L^2 + \dot{\phi}_R^2] + \frac{1}{2} \frac{C_J^B}{C_J} \frac{(\dot{\phi}^B)^2}{\omega_J^2} \right. \\ & - \frac{1}{2} \frac{L \lambda_J^2}{\hat{L} a^2} (\phi_R - \phi_L + \phi^B)^2 \\ & \left. + \frac{\hat{I}_c - I_c}{I_c} [\cos \phi_L + \cos \phi_R] + \frac{I_c^B}{I_c} \cos \phi^B \right\}. \quad (\text{B4}) \end{aligned}$$

Here, we have included charging and Josephson energy for extra junctions with phases $\phi_{N_l} = \phi_L$ and $\phi_{N_l+1} = \phi_R$ to the LJJ's in Eqs. (B2) and (B3). To correct for this, the same charging energy $\propto C_J$ and Josephson energy $\propto I_c$ are subtracted in Eq. (B4) for the interface. This allows us to replace the LJJ sums in the continuum limit $a/\lambda_J \rightarrow 0$ by integrals with boundaries $(-\infty, 0)$ and $(0, \infty)$. Inserting ϕ and $\dot{\phi}$ from Eq. (5) these integrations yield

$$\tilde{\mathcal{L}}_l + \tilde{\mathcal{L}}_r = \sum_{i=L,R} \frac{m_0(X_i) \dot{X}_i^2}{2c^2} - U_0(X_L, X_R), \quad (\text{B5})$$

$$\begin{aligned} U_0 = & \sum_{i=L,R} \frac{4\lambda_J}{W} \left(1 - \frac{2z_i}{\sinh(2z_i)} \right) \\ & + \frac{2W}{\lambda_J} \tanh(z_i) \operatorname{sech}^2(z_i) [2z_i + \sinh(2z_i)], \quad (\text{B6}) \end{aligned}$$

$$m_0(X_i) = \frac{8\lambda_J}{W} \left(1 + \frac{2z_i}{\sinh(2z_i)} \right) \quad (\text{B7})$$

with $z_i = X_i/W$ ($i = L, R$), and dimensionless potential $U_0(X_L, X_R)$ and masses $m_0(X_i)$. $U_0(X_L, X_R)$ is shown in Fig. 12(a).

From Eq. (1) [or Eqs. (B1)–(B4)] we obtain the equations of motion for the interface junctions

$$\frac{\hat{C}_J}{C_J} \frac{\ddot{\phi}_L}{\omega_J^2} = \frac{\lambda_J^2 L}{a^2 \hat{L}} \zeta - \frac{\lambda_J}{a} \frac{\phi_L - \phi_{N_l-1}}{a/\lambda_J} - \frac{\hat{I}_c}{I_c} \sin \phi_L, \quad (\text{B8})$$

$$\frac{\hat{C}_J}{C_J} \frac{\ddot{\phi}_R}{\omega_J^2} = -\frac{\lambda_J^2 L}{a^2 \hat{L}} \zeta + \frac{\lambda_J}{a} \frac{\phi_{N_l+2} - \phi_R}{a/\lambda_J} - \frac{\hat{I}_c}{I_c} \sin \phi_R, \quad (\text{B9})$$

$$\frac{C_J^B}{C_J} \frac{\ddot{\phi}^B}{\omega_J^2} = -\frac{\lambda_J^2 L}{a^2 \hat{L}} \zeta - \frac{I_c^B}{I_c} \sin \phi^B, \quad (\text{B10})$$

where we have introduced $\zeta = (\phi_R - \phi_L + \phi^B)$. We are interested in the regime of $(L\lambda_J^2)/(\hat{L}a^2) \gg \hat{C}_J/C_J$, λ_J/a , \hat{I}_c/I_c , C_J^B/C_J , I_c^B/I_c . This allows us to treat Eqs. (B8)–(B10) in perturbation expansion, with the small parameter $(\hat{L}a^2)/(L\lambda_J^2)$. The leading-order contribution has $\zeta = 0$, i.e., $\phi^B = \phi_L - \phi_R$, while ϕ_L , ϕ_R , ϕ^B occurring individually in Eqs. (B8)–(B10) have finite leading-order contributions. One can then use Eq. (B10) to determine the next-to-leading-order contribution of ζ , $(L\lambda_J^2)/(\hat{L}a^2)\zeta = -C_J^B/(C_J\omega_J^2)\ddot{\phi}^B - (I_c^B/I_c)\sin\phi^B$. Inserting

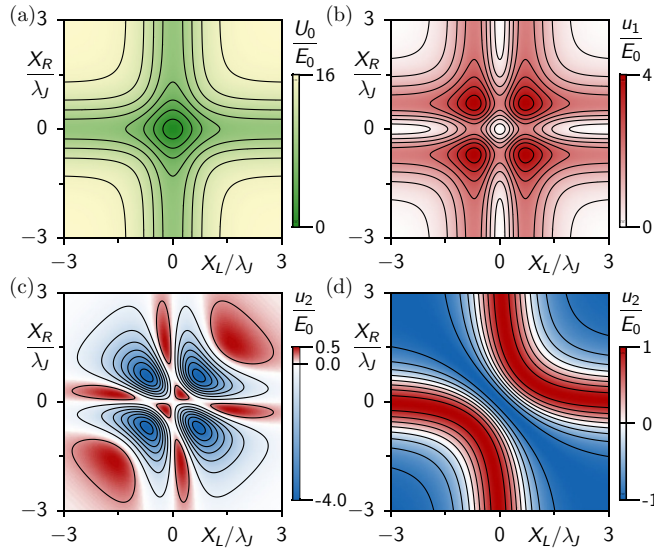


FIG. 12. Contributions to CC potential U vs X_L, X_R . (a) LJJ contribution U_0 [Eq. (B6)] and interface contributions for one-bit interface with one center junction: (b) u_1 [Eq. (B17)], and (c) u_2 [Eq. (B18)]. For one-bit interface with two center junctions U_0 and u_1 are identical to above, while (d) u_2 differs [Eq. (B29)].

this in the remaining Eqs. (B8) and (B9), we obtain equations of motion for ϕ_L and ϕ_R in leading order. This reduced dynamical system is still described by the Lagrangian (B1), but the interface Lagrangian now takes the form

$$\begin{aligned} \tilde{\mathcal{L}}_I = & \frac{\hat{C}_J - C_J + C_J^B}{2C_J\omega_J^2\lambda_J/a} [\dot{\phi}_L^2 + \dot{\phi}_R^2] - \frac{C_J^B}{C_J\lambda_J/a} \frac{\dot{\phi}_L\dot{\phi}_R}{\omega_J^2} \\ & + \frac{\hat{I}_c - I_c}{I_c\lambda_J/a} [\cos\phi_L + \cos\phi_R] + \frac{I_c^B}{I_c\lambda_J/a} \cos(\phi_L - \phi_R). \end{aligned} \quad (\text{B11})$$

Inserting ϕ and $\dot{\phi}$ from Eq. (5) into Eq. (B11), where we approximate $\phi_L \approx \phi(x=0^-)$ and $\phi_R \approx \phi(x=0^+)$, we calculate the interface contribution to the Lagrangian, which then reads as

$$\tilde{\mathcal{L}} = \frac{m_L\dot{X}_L^2}{2c^2} + \frac{m_R\dot{X}_R^2}{2c^2} + m_{LR} \frac{\dot{X}_L\dot{X}_R}{c^2} - U(X_L, X_R), \quad (\text{B12})$$

$$U = U_0 + \frac{\hat{I}_c - I_c + I_c^B}{I_c\lambda_J/a} u_1 + \frac{I_c^B}{I_c\lambda_J/a} u_2, \quad (\text{B13})$$

with coordinate-dependent masses

$$m_i(X_i) = m_0(X_i) + \frac{\hat{C}_J - C_J + C_J^B}{C_J\lambda_J/a} (g_I(X_i))^2 \quad (\text{B14})$$

and coupling mass

$$m_{LR}(X_L, X_R) = \frac{C_J^B}{C_J\lambda_J/a} g_I(X_L)g_I(X_R), \quad (\text{B15})$$

$$g_I(X_i) = 4(\lambda_J/W) \operatorname{sech}(X_i/W) \quad (\text{B16})$$

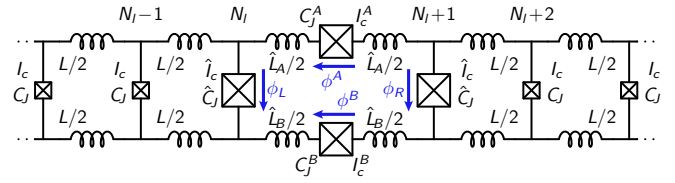


FIG. 13. A one-bit gate connecting two LJJs that has two center junctions. This circuit is also introduced in Fig. 10(b) by the equivalence to a two-bit circuit.

[compare Eqs. (8)–(11)]. The interface contributions to the potential are

$$u_1 = \sum_{i=L,R} 8 \operatorname{sech}^2(z_i) \tanh^2(z_i), \quad (\text{B17})$$

$$\begin{aligned} u_2 = & - \prod_{i=L,R} [8 \operatorname{sech}^2(z_i) \tanh^2(z_i)] \\ & + \prod_{i=L,R} [4 \operatorname{sech}(z_i) \tanh(z_i) [1 - 2 \operatorname{sech}^2(z_i)]], \end{aligned} \quad (\text{B18})$$

and are shown in Figs. 12(b) and 12(c). The potential $U(X_L, X_R)$ is symmetric under the coordinate exchange $X_L \leftrightarrow X_R$. The contributions U_0 and u_1 have even parity under each of the transformations $X_i \leftrightarrow -X_i$ ($i = L, R$), while $u_2(X_L, X_R)$ has no parity symmetry.

2. Interface with two center junctions (2-JJ)

Here, we consider a modified one-bit interface, shown in Fig. 13. It is similar to that in Fig. 1(a), but has a center junction in the A line of the interface as well as in the B line. The phase difference ϕ^A over this junction provides an additional degree of freedom, and instead of Eq. (B4) the interface Lagrangian becomes

$$\begin{aligned} \tilde{\mathcal{L}}_I = & \frac{a}{\lambda_J} \left\{ \frac{\hat{C}_J - C_J}{2C_J\omega_J^2} [\dot{\phi}_L^2 + \dot{\phi}_R^2] + \frac{C_J^A(\dot{\phi}^A)^2 + C_J^B(\dot{\phi}^B)^2}{2C_J\omega_J^2} \right. \\ & - \frac{L\lambda_J^2}{2(\hat{L}_A + \hat{L}_B)a^2} (\phi_R - \phi_L - \phi^A + \phi^B)^2 \\ & \left. + \frac{\hat{I}_c - I_c}{I_c} [\cos\phi_L + \cos\phi_R] + \frac{I_c^B}{I_c} \cos\phi^B + \frac{I_c^A}{I_c} \cos\phi^A \right\}, \end{aligned} \quad (\text{B19})$$

where $\hat{L}_{A,B}$ are the interface inductances. For brevity, we refer to the interface of Fig. 13 as the 2-JJ interface, and to that of Fig. 1(a) as the 1-JJ interface.

Approximate equivalence to 1-JJ interface. For simplicity, we also only discuss the case of vertical symmetry, with $C_J^A = C_J^B$ and $I_c^A = I_c^B$. Under this condition, Eq. (B19) generates the equation of motion

$$2C_J^A \ddot{\psi} = -2I_c^A \sin\psi \cos[(\phi^A - \phi^B)/2] \quad (\text{B20})$$

for the phase average

$$\psi = (\phi^A + \phi^B)/2. \quad (\text{B21})$$

In our simulations, the interface initially has $\psi = 0$. From Eq. (B20) it follows that $\psi = 0$ is a fixed point of the dynamics, such that we may set $\psi = 0$ in Eq. (B19), which then becomes

$$\begin{aligned} \tilde{\mathcal{L}}_I = & \frac{a}{\lambda_J} \left\{ \frac{\hat{C}_J - C_J}{2C_J\omega_J^2} [\dot{\phi}_L^2 + \dot{\phi}_R^2] + \frac{2C_J^A(\dot{\phi}^A)^2}{2C_J\omega_J^2} \right. \\ & - \frac{L\lambda_J^2}{2(\hat{L}_A + \hat{L}_B)a^2} (\phi_R - \phi_L - 2\phi^A)^2 \\ & \left. + \frac{\hat{I}_c - I_c}{I_c} [\cos \phi_L + \cos \phi_R] + \frac{2I_c^A}{I_c} \cos \phi^A \right\}. \end{aligned} \quad (\text{B22})$$

To compare this expression with the Lagrangian of the 1-JJ interface, Eq. (B4), we first ignore the Josephson potentials. The 2-JJ interface with two (identical) center junctions and values $(\hat{L}_A + \hat{L}_B, \phi^A, C_J^A)$ then maps exactly to the equivalent 1-JJ interface and values $(\hat{L}, -\phi^B/2, 2C_J^B)$. Further analyzing the Josephson potentials to quadratic order in the phases we find that the critical current I_c^A in the 2-JJ interface corresponds to a critical current $2I_c^B$ in the equivalent 1-JJ interface. That means that the scattering at the (approximately) equivalent 1-JJ and 2-JJ interfaces is very similar, provided that either ϕ^B remains small, or the critical currents are small, $I_c^B \ll \hat{I}_c, I_c$.

CC analysis. Now, we perform the CC analysis for the 2-JJ interface. To this end, we go back to Eq. (B19), where we again assume vertical symmetry of the interface, but allow for finite ψ . Once again, we restrict ourselves to the perturbative case of small interface inductance $(\hat{L}_A + \hat{L}_B) \ll L\lambda_J^2/a^2$. To leading order we obtain the constraint $\phi^A - \phi^B = \phi_R - \phi_L$ for the interface cell such that ϕ^A and ϕ^B can be expressed through $\phi_R - \phi_L$ and ψ . With these replacements, Eq. (B19) reads as

$$\begin{aligned} \tilde{\mathcal{L}}_I = & \frac{\hat{C}_J - C_J + C_J^A/2}{2C_J\omega_J^2\lambda_J/a} [\dot{\phi}_L^2 + \dot{\phi}_R^2] - \frac{C_J^A/2}{C_J\lambda_J/a} \frac{\dot{\phi}_L\dot{\phi}_R}{\omega_J^2} \\ & + \frac{\hat{I}_c - I_c}{I_c\lambda_J/a} [\cos \phi_L + \cos \phi_R] + \frac{C_J^A}{C_J\lambda_J/a} \frac{\dot{\psi}^2}{\omega_J^2} \\ & + \frac{2I_c^A}{I_c\lambda_J/a} \cos \psi \cos \left(\frac{\phi_L - \phi_R}{2} \right). \end{aligned} \quad (\text{B23})$$

From Eq. (B1) together with (B23) the CC Lagrangian is derived (similar to Appendix B 1),

$$\tilde{\mathcal{L}} = \frac{m_L}{2} \frac{\dot{X}_L^2}{c^2} + \frac{m_R}{2} \frac{\dot{X}_R^2}{c^2} + m_{LR} \frac{\dot{X}_L\dot{X}_R}{\omega_J^2} + \frac{m_\psi}{2} \dot{\psi}^2 - U(X_L, X_R), \quad (\text{B24})$$

$$U = U_0 + \frac{\hat{I}_c - I_c}{I_c\lambda_J/a} u_1 + \frac{2I_c^A}{I_c\lambda_J/a} \cos(\psi) u_2, \quad (\text{B25})$$

$$m_i = m_0(X_i) + \frac{\hat{C}_J - C_J + C_J^A/2}{C_J\lambda_J/a} (g_I(X_i))^2, \quad (\text{B26})$$

$$m_{LR} = \frac{C_J^A/2}{C_J\lambda_J/a} g_I(X_L)g_I(X_R), \quad (\text{B27})$$

$$m_\psi = \frac{2C_J^A}{C_J\lambda_J/a} \quad (\text{B28})$$

with U_0 , u_1 , m_0 , and g_I identical to expressions for the 1-JJ interface [Eqs. (B6), (B17), (B7), and (B16)]. The I_c^B -proportional contribution to the interface potential is

$$\begin{aligned} u_2 = & - \prod_{i=L,R} [\text{sech}^2(z_i) - \tanh^2(z_i)] \\ & + 4 \prod_{i=L,R} \text{sech}(z_i) \tanh(z_i), \end{aligned} \quad (\text{B29})$$

and is shown in Fig. 12(d). It differs qualitatively from the u_2 for the 1-JJ interface, which is given in Eq. (B18) and Fig. 12(c).

The form of the reduced dynamical system for X_L, X_R remains invariant [Eqs. (13)–(15)], but here an additional equation of motion exists for ψ :

$$\ddot{\psi} = -\omega_J^2 \frac{\partial U}{\partial \psi} = \frac{2I_c^B}{I_c\lambda_J/a} \sin(\psi) u_2. \quad (\text{B30})$$

Again, starting from the fixed point $\psi = 0$, the CC dynamics can be compared with that of the 1-JJ interface. To this end, we substitute parameters as above for the (approximately) equivalent 1-JJ interface. With this substitution, most CC quantities become equal to those in Eqs. (B12)–(B17). One exception is the different form of the interface potential u_2 , as mentioned above. Another exception is the prefactor of the interface potential u_1 . While in the 1-JJ interface u_1 has a weighting $\propto I_c^B$ [Eq. (B13)], no equivalent weighting $\propto I_c^A$ appears in Eq. (B25). In this study, we focus on the case $I_c^B \ll I_c$ where these differences in the potential U are negligible, and the fluxon scattering at the (approximately) equivalent 1- and 2-JJ interfaces are therefore very similar.

APPENDIX C: MAPPING TWO-BIT GATE TO ONE-BIT GATES

Here, we discuss the Lagrangian for the interface which connects two LJJs from each side [Fig. 10(a)]. The interface is assumed to be both left-right and vertically symmetric. Using the notation ϕ^{AB} and ϕ^{BC} for the phases across the upper and lower LJJs, respectively, the interface Lagrangian $\tilde{\mathcal{L}}_I$ is

$$\begin{aligned} \tilde{\mathcal{L}}_I = & \frac{a}{\lambda_J} \left\{ \frac{1}{2} \frac{\hat{C}_J - C_J}{C_J\omega_J^2} \sum_s [(\dot{\phi}_L^s)^2 + (\dot{\phi}_R^s)^2] + \frac{C_J^B}{2C_J} \frac{(\dot{\phi}^B)^2}{\omega_J^2} \right. \\ & + \frac{C_J^A}{2C_J} \frac{(\dot{\phi}^A)^2 + (\dot{\phi}^C)^2}{\omega_J^2} + \frac{I_c^A}{I_c} [\cos \phi^A + \cos \phi^C] \\ & - \left(\frac{2\pi}{\Phi_0} \right)^2 \frac{L\lambda_J^2}{2a^2} [\hat{L}^A(\hat{I}^A)^2 + \hat{L}^B(\hat{I}^B)^2 + \hat{L}^A(\hat{I}^C)^2] \\ & \left. + \frac{\hat{I}_c - I_c}{I_c} \sum_s [\cos \phi_L^s + \cos \phi_R^s] + \frac{I_c^B}{I_c} \cos \phi^B \right\} \end{aligned} \quad (\text{C1})$$

($s = AB, BC$). Without DC bias from the left to the right of the gate, the currents in the interface lines fulfill $\hat{I}^A + \hat{I}^B + \hat{I}^C = 0$, and

$$\begin{aligned} \hat{I}^A = & \frac{\Phi_0/(2\pi)}{\hat{L}^A(\hat{L}^A + 2\hat{L}^B)} [-(\hat{L}^A + \hat{L}^B)\phi^A + \hat{L}^A\phi^B + \hat{L}^B\phi^C \\ & + (\hat{L}^A + \hat{L}^B)(\phi_R^{AB} - \phi_L^{AB}) + \hat{L}^B(\phi_R^{BC} - \phi_L^{BC})], \end{aligned} \quad (\text{C2})$$

$$\begin{aligned} \hat{f}^C = & \frac{\Phi_0/(2\pi)}{\hat{L}^A(\hat{L}^A + 2\hat{L}^B)} [\hat{L}^B \phi^A + \hat{L}^A \phi^B - (\hat{L}^A + \hat{L}^B) \phi^C \\ & - \hat{L}^B (\phi_R^{AB} - \phi_L^{AB}) - (\hat{L}^A + \hat{L}^B) (\phi_R^{BC} - \phi_L^{BC})]. \end{aligned} \quad (\text{C3})$$

Similar to the one-bit interfaces, we consider the limit of small interface inductances $\hat{L}^{A,B}$, which here results in the interface-cell constraints $\phi^A - \phi^B = \phi_R^{AB} - \phi_L^{AB}$ and $\phi^B - \phi^C = \phi_R^{BC} - \phi_L^{BC}$. The third line in Eq. (C1) then becomes negligible.

We discuss the cases of initially equivalent fields in the upper and lower LJJ, $\phi_n^{BC} = \pm \phi_n^{AB}$. Coupling between ϕ^{AB} and ϕ^{BC} occurs only within the interface. We start with the assumption that $\phi^{BC} = \phi^{AB}$ or $\phi^{BC} = -\phi^{AB}$ remains fulfilled throughout the evolution. This will be confirmed below by the effective decoupling of the upper and lower interface cells imposed by the symmetry.

Case I, $\phi^{BC} = \phi^{AB}$. The symmetry together with the above cell constraints give $\phi^A - 2\phi^B + \phi^C = 0$. The current on the B line cancels, $\hat{I}^B = 0$. For symmetry reasons, $\phi^C = -\phi^A$, and thus $\phi^B = 0$. Therefore, the interface Lagrangian (C1) is a sum of two independent contributions

$$\tilde{\mathcal{L}}_I = \tilde{\mathcal{L}}_I^{AB} + \tilde{\mathcal{L}}_I^{BC}, \quad (\text{C4})$$

with

$$\begin{aligned} \tilde{\mathcal{L}}_I^{AB} = & \frac{a}{\lambda_J} \left\{ \frac{\hat{C}_J - C_J}{2C_J \omega_J^2} [(\dot{\phi}_L^{AB})^2 + (\dot{\phi}_R^{AB})^2] + \frac{C_J^A}{2C_J} \frac{(\dot{\phi}^A)^2}{\omega_J^2} \right. \\ & \left. + \frac{\hat{I}_c - I_c}{I_c} [\cos \phi_L^{AB} + \cos \phi_R^{AB}] + \frac{I_c^A}{I_c} \cos \phi^A \right\}, \end{aligned} \quad (\text{C5})$$

and $\tilde{\mathcal{L}}_I^{BC}$ given by the same expression but with the substitutions $AB \rightarrow BC$, $\phi^{AB} \rightarrow \phi^{BC}$, and $\phi^A \rightarrow -\phi^C$. Since there is no coupling term, ϕ^{AB} and ϕ^{BC} effectively evolve independently. Because of vertical symmetry of the interface, the initial relation $\phi^{AB}(0) = \phi^{BC}(0)$ remains fulfilled for all times,

i.e., the fields remain synchronized. Each of the Lagrangians $\tilde{\mathcal{L}}_I^s$ is identical to that of an equivalent one-bit interface with one center junction, Eq. (B4), which has characteristic values (C_J^A, I_c^A) , as indicated in Fig. 10(b). Note that the equivalence to the one-bit interface holds also for finite interface inductances \hat{L}^A, \hat{L}^B , which we have neglected here for simplicity. The inductance \hat{L} of the equivalent one-bit interface is then given by \hat{L}_A .

Case II, $\phi^{BC} = -\phi^{AB}$. Here, the cell constraints imply that $\phi^A = \phi^C$. Again, Eq. (C1) is a sum of two independent contributions, with

$$\begin{aligned} \tilde{\mathcal{L}}_I^{AB} = & \frac{a}{\lambda_J} \left\{ \frac{1}{2} \frac{\hat{C}_J - C_J}{C_J \omega_J^2} [(\dot{\phi}_L^{AB})^2 + (\dot{\phi}_R^{AB})^2] + \frac{C_J^A}{2C_J} \frac{(\dot{\phi}^A)^2}{\omega_J^2} \right. \\ & + \frac{C_J^B}{4C_J} \frac{(\dot{\phi}^B)^2}{\omega_J^2} + \frac{I_c^B}{2I_c} \cos \phi^B \\ & \left. + \frac{\hat{I}_c - I_c}{I_c} [\cos \phi_L^{AB} + \cos \phi_R^{AB}] + \frac{I_c^A}{I_c} \cos \phi^A \right\}, \end{aligned} \quad (\text{C6})$$

where $\phi^B = \phi^A - \phi_R^{AB} + \phi_L^{AB}$. The same expression defines $\tilde{\mathcal{L}}_I^{BC}$, but with the substitutions $AB \rightarrow BC$, $\phi^{AB} \rightarrow -\phi^{BC}$, and $\phi^A \rightarrow \phi^C$. Each $\tilde{\mathcal{L}}_I^s$ is identical to the Lagrangian of an equivalent one-bit interface with two center junctions [Eq. (B19)], as indicated in Fig. 10(c). The equivalent center junctions have characteristic values (C_J^A, I_c^A) and $(C_J^B/2, I_c^B/2)$, respectively. Also, the sum of interface inductances in the equivalent one-bit 2-JJ interface, $\hat{L}_A + \hat{L}_B$, equals $\hat{L}_A + 2\hat{L}_B$ from the two-bit interface.

If this equivalent one-bit 2-JJ interface, moreover, has vertical symmetry, i.e., if $C_J^A = C_J^B/2$, $I_c^A = I_c^B/2$, then we can approximately map further to a one-bit 1-JJ interface, as discussed in Appendix B 2. This approximately equivalent interface has center-junction values $(C_J^A/2, I_c^A/2)$ and center inductance \hat{L} of $\hat{L}_A + 2\hat{L}_B$.

-
- [1] International roadmap for devices and systems, 2017, <https://irds.ieee.org/roadmap-2017>.
- [2] T. N. Theis and H.-S. P. Wong, *Comput. Sci. Eng.* **19**, 41 (2017).
- [3] K. K. Likharev and V. K. Semenov, *IEEE Trans. Appl. Supercond.* **1**, 3 (1991).
- [4] Q. P. Herr, A. Y. Herr, O. T. Oberg, and A. G. Ioannidis, *J. Appl. Phys.* **109**, 103903 (2011).
- [5] Anna Herr (private communication).
- [6] D. S. Holmes, A. L. Ripple, and M. A. Manheimer, *IEEE Trans. Appl. Supercond.* **23**, 1701610 (2013).
- [7] C. H. Bennett, *IBM J. Res. Dev.* **17**, 525 (1973).
- [8] K. K. Likharev, *Int. J. Theor. Phys.* **21**, 311 (1982).
- [9] J. Ren and V. K. Semenov, *IEEE Trans. Appl. Supercond.* **21**, 780 (2011).
- [10] N. Takeuchi, Y. Yamanashi, and N. Yoshikawa, *Sci. Rep.* **4**, 6354 (2014).
- [11] N. Takeuchi and Y. Yamanashi, and N. Yoshikawa, *Phys. Rev. Appl.* **4**, 034007 (2015).
- [12] E. Fredkin and T. Toffoli, *Int. J. Theor. Phys.* **21**, 219 (1982).
- [13] M. N. Islam and C. E. Socolich, *Opt. Lett.* **16**, 1490 (1991).
- [14] J. Scheuer and M. Orenstein, *J. Opt. Soc. Am. B* **22**, 1260 (2005).
- [15] P. D. Drummond and W. Man, *Opt. Commun.* **105**, 99 (1994).
- [16] D. W. McLaughlin and A. C. Scott, *Phys. Rev. A* **18**, 1652 (1978).
- [17] F. Zhang, Y. S. Kivshar, and L. Vázquez, *Phys. Rev. A* **45**, 6019 (1992).
- [18] R. H. Goodman and R. Haberman, *Phys. Rev. Lett.* **98**, 104103 (2007).
- [19] D. V. Averin, K. Rabenstein, and V. K. Semenov, *Phys. Rev. B* **73**, 094504 (2006).
- [20] K. G. Fedorov, A. V. Shcherbakova, M. J. Wolf, D. Beckmann, and A. V. Ustinov, *Phys. Rev. Lett.* **112**, 160502 (2014).
- [21] A. Fedorov, A. Shnirman, G. Schön, and A. Kidiyarova-Shevchenko, *Phys. Rev. B* **75**, 224504 (2007).
- [22] I. I. Soloviev, N. V. Klenov, A. L. Pankratov, L. S. Revin, E. Il'ichev, and L. S. Kuzmin, *Phys. Rev. B* **92**, 014516 (2015).
- [23] K. D. Osborn and W. Wustmann, *Reversible Computation*, RC 2018, Lecture Notes in Computer Science (Springer, Cham, 2018), Vol. 11106, p. 189.

- [24] T. Dauxois and M. Peyrard, *Physics of Solitons* (Cambridge University Press, Cambridge, 2006).
- [25] A. C. Newell, *Solitons in Mathematics and Physics* (Society for Industrial and Applied Mathematics, Philadelphia, 1985).
- [26] O. M. Braun and Y. S. Kivshar, *Phys. Rep.* **306**, 1 (1998).
- [27] J. Pfeiffer, A. A. Abdumalikov, Jr., M. Schuster, and A. V. Ustinov, *Phys. Rev. B* **77**, 024511 (2008).
- [28] M. Peyrard and M. D. Kruskal, *Phys. D (Amsterdam)* **14**, 88 (1984).
- [29] A. Barone and G. Paternò, *Physics and Applications of the Josephson Effect* (Wiley, New York, 1982).
- [30] S. K. Tolpygo, *Low Temp. Phys.* **42**, 361 (2016).
- [31] G. Costabile, R. D. Parmentier, B. Savo, D. W. McLaughlin, and A. C. Scott, *Appl. Phys. Lett.* **32**, 587 (1978).
- [32] S. Ghoshal and A. Zamolodchikov, *Int. J. Mod. Phys. A* **09**, 3841 (1994).
- [33] T. Van Duzer and C. W. Turner, *Principles of Superconductive Devices and Circuits* (Prentice Hall, Upper Saddle River, NJ, 1999).